

# A RECYCLING TRAINING STRATEGY FOR MEDICAL IMAGE SEGMENTATION WITH DIFFUSION DENOISING MODELS

A PREPRINT

✉ **Yunguan Fu**  
 University College London  
 InstaDeep

✉ **Yiwen Li**  
 University of Oxford

✉ **Shaheer U. Saeed**  
 University College London

✉ **Matthew J. Clarkson**  
 University College London

✉ **Yipeng Hu**  
 University College London

## ABSTRACT

Denoising diffusion models have found applications in image segmentation by generating segmented masks conditioned on images. Existing studies predominantly focus on adjusting model architecture or improving inference such as test-time sampling strategies. In this work, we focus on training strategy improvements and propose a novel recycling method. During each training step, a segmentation mask is first predicted given an image and a random noise. This predicted mask, replacing the conventional ground truth mask, is used for denoising task during training. This approach can be interpreted as aligning the training strategy with inference by eliminating the dependence on ground truth masks for generating noisy samples. Our proposed method significantly outperforms standard diffusion training, self-conditioning, and existing recycling strategies across multiple medical imaging data sets: muscle ultrasound, abdominal CT, prostate MR, and brain MR. This holds true for two widely adopted sampling strategies: denoising diffusion probabilistic model and denoising diffusion implicit model. Importantly, existing diffusion models often display a declining or unstable performance during inference, whereas our novel recycling consistently enhances or maintains performance. Furthermore, we show for the first time that, under a fair comparison with the same network architectures and computing budget, the proposed recycling-based diffusion models achieved on-par performance with non-diffusion-based supervised training. This paper summarises these quantitative results and discusses their values, with a fully reproducible JAX-based implementation, released at <https://github.com/mathpluscode/ImgX-DiffSeg>.

## 1 Introduction

Diffusion denoising models, first proposed by Sohl-Dickstein et al. [2015], Ho et al. [2020], Ho and Salimans [2022], are generative models that produce data samples via iterative denoising processes. These models achieved superior performance compared to generative adversarial networks [Goodfellow et al., 2020] and became the foundation for many image generation applications such as DALL·E 2 [Ramesh et al., 2022], stable diffusion, and Midjourney [Rombach et al., 2022], etc. Given the success in computer vision, diffusion models have been adapted in medical imaging across various fields, including image synthesis [Dorjsembe et al., 2022, Khader et al., 2022], image denoising [Hu et al., 2022], anomaly detection [Wolleb et al., 2022a], classification [Yang et al., 2023], segmentation [Wu et al., 2022, Rahman et al., 2023], and registration [Kim et al., 2022]. Among these, segmentation is one of the most foundational tasks in medical imaging and a variety of applications have been explored, including liver CT [Xing et al., 2023], lung CT [Zbinden et al., 2023, Rahman et al., 2023], abdominal CT [Wu et al., 2023, Fu et al., 2023], brain MR [Pinaya et al., 2022a, Wolleb et al., 2022b, Wu et al., 2023, Xing et al., 2023, Bieder et al., 2023], and prostate MR [Fu et al., 2023].

For segmentation tasks, even though various model architectures and training strategies [Wang et al., 2022] have been proposed, U-net equipped with attention mechanisms and trained by supervised learning consistently remains the state-of-the-art model and an important baseline. In comparison, divergent observations have arisen: certain studies

reported superior performance of diffusion-based segmentation models [Amit et al., 2021, Wu et al., 2022, 2023, Xing et al., 2023], while others observed the opposite trend [Pinaya et al., 2022a, Wolleb et al., 2022b, Kolbeinsson and Mikolajczyk, 2022, Fu et al., 2023]. This inconsistency may result from different training schemes, network architectures, and application-specific modifications in comparisons, suggesting that challenges still persist in applying diffusion models for image segmentation.

Formally, conditioning on an image, diffusion-based segmentation models operate by progressive denoising, starting with a random noise and ultimately yielding the corresponding segmentation masks. In comparison to their non-diffusion counterparts, the necessity of supplementary noisy masks as input leads to increased memory demands that can pose challenges, particularly for processing 3D volumetric medical images. To address this, volume slicing [Wu et al., 2023] or patching [Xing et al., 2023, Bieder et al., 2023] has been used to manage memory limitations. However, diffusion model training still requires considerable computation due to its inherent iterative nature, since the same model needs to learn to denoise masks with varying levels of noise. Consequently, enhancing the diffusion model performance while adhering to a fixed compute budget is of significant importance. Empirically, using the reparametrisation [Kingma et al., 2021], the denoising training task has shifted from noise prediction [Wolleb et al., 2022b, Wu et al., 2022] to mask prediction [Fu et al., 2023, Zbinden et al., 2023] due to the superior performance and faster learning. Furthermore, Fu et al. [2023] highlighted a limitation of diffusion models, noting the misalignment between the training and inference procedures since the training samples were generated from ground truth masks. This raises concerns of data leakage as discussed in Chen et al. [2022a]. However, there have been limited studies in medical image segmentation that rigorously compare diffusion models with their non-diffusion counterparts and examine diffusion training efficiency.

In this work, we focus on an application-agnostic improvement of the training strategy for diffusion denoising models that is applicable to 2D and 3D medical image segmentation across different modalities. A novel recycling training strategy is proposed. At each training step, a segmentation prediction is first produced, given the image and a fully noise-corrupted mask. The predicted mask, substituting the conventional ground truth mask, is then used for denoising training. Notably, our approach distinguishes itself from the existing recycling method [Fu et al., 2023] by employing a fully corrupted mask in the first step, reducing the reliance on ground truth information. The recycling strategy also differs from the self-conditioning techniques proposed in Chen et al. [2022b], Watson et al. [2023], as noisy samples in self-conditioning are based on ground truth while recycling relies on predicted mask instead. By testing on four large data sets – 2D muscle ultrasound with 3910 images, 3D abdominal CT with 300 images, 3D prostate MR with 589 images and 3D brain MR with 1251 images – the novel recycling strategy enables the diffusion models to refine or maintain the segmentation accuracy throughout the inference process. In contrast, all other diffusion models demonstrate declining or unstable performance trends. Our proposed method significantly outperformed these diffusion training strategies across all data sets for both denoising diffusion probabilistic model-based [Ho et al., 2020] and denoising diffusion implicit model-based [Song et al., 2020a] sampling procedures. Compared to non-diffusion-based supervised U-net, the proposed diffusion models achieved similar performance with identical network architectures, training schemes, and compute budgets. The value of an alternative segmentation method with comparable performance has also been discussed. The JAX-based framework has been released on <https://github.com/mathpluscode/ImgX-DiffSeg>.

## 2 Related Works

The diffusion process is a Markov process where data structures are gradually noise-corrupted and eventually destroyed (noising process). A reverse diffusion process (denoising process) can then be learned, where the objective is to gradually recover the data structure. Sohl-Dickstein et al. [2015] first proposed diffusion models which map the disrupted data to a noise distribution. Ho et al. [2020] have shown that such modelling is equivalent to score-matching models, a class of models that estimates the gradient of the log-density [Hyvärinen and Dayan, 2005, Vincent, 2011, Song and Ermon, 2019, 2020]. This led to a simplified variational lower bound training objective and a denoising diffusion probabilistic model (DDPM) [Ho et al., 2020]. DDPM achieved state-of-the-art performance for unconditional image generation on CIFAR10 at the time. In practice, DDPMs were found suboptimal on log-likelihood estimation and Nichol and Dhariwal [2021] addressed this with a learnable variance schedule, sinusoidal noise schedule, and an importance sampling for time steps. Furthermore, diffusion models were trained with hundreds or thousands of steps, inference with the same number of steps is time-consuming. Different strategies have therefore been proposed to enable faster sampling. While Nichol and Dhariwal [2021] suggested a variance resampling without modifying the probabilistic distribution, Song et al. [2020a] derived a deterministic model, denoising diffusion implicit model (DDIM), which shares the same marginal distribution as DDPM. Liu et al. [2022] further generalised the reverse step of DDIM into an ordinary differential equation and used high-order numerical methods (e.g. Runge-Kutta method) with predicted noise to perform sampling with second-order convergence. Besides, Zheng et al. [2022], Lyu et al. [2022], Guo et al. [2022] accelerate diffusion model training by shortening the noising schedule and only considering a truncated diffusion chain with less noise. These unconditioned denoising diffusion models have been successfully applied in multiple

medical imaging applications [Kazerouni et al., 2023], including brain MR image generation [Dorjsembe et al., 2022, Khader et al., 2022], optical coherence tomography denoising [Hu et al., 2022], and chest X-ray pleural effusion detection [Wolleb et al., 2022a].

Guided diffusion models have been developed to generate data in a controllable manner. Song et al. [2020b], Dhariwal and Nichol [2021] used gradients of pre-trained classifiers to bias the sampling process, without modifying the diffusion model training. Ho and Salimans [2022], on the other hand, modified the models to take additional information as input, enabling end-to-end conditional diffusion model training. For medical image synthesis, conditions can be patient biometric information [Pinaya et al., 2022b], genotypes data [Moghadam et al., 2023], or images from different modalities [Saeed et al., 2023]. Conditional diffusion models have also been explored for medical image classification [Yang et al., 2023], segmentation [Wu et al., 2022, Rahman et al., 2023], and registration [Kim et al., 2022]. Particularly for image segmentation, the diffusion models apply the noising and denoising on the segmentation masks and the network takes a noisy mask and an image to perform denoising.

In contrast to the continuous spectrum of values found in natural images, image segmentation mask values are categorical and nominal. The Gaussian-based continuous diffusion processes behind DDPM and DDIM cannot be directly applied. Chen et al. [2022b] therefore encoded categories with binary bits and relaxed them to real values for continuous diffusion models. Han et al. [2022], Fu et al. [2023] encoded categories with one-hot embeddings and performed diffusion on scaled values. Li et al. [2022a], Strudel et al. [2022] encoded the discrete data and applied diffusion processes in embedding spaces directly. Alternatively, discrete diffusion models have been proposed to model the transition matrix between categories based on discrete probability distributions, including binomial distribution [Sohl-Dickstein et al., 2015], categorical distribution [Hoogeboom et al., 2021, Austin et al., 2021, Gu et al., 2022], and Bernoulli distribution [Chen et al., 2023]. In this work, we follow Fu et al. [2023] to perform diffusion on scaled binary masks.

Originally, DDPM models were trained via noise prediction [Ho et al., 2020], where the loss was calculated between predicted and sampled noises. Many diffusion-based segmentation models directly adopted this strategy [Wolleb et al., 2022b, Wu et al., 2022]. Alternatively, Kingma et al. [2021] derived an equivalent formulation (often known as  $x_0$  reparameterisation) of the variational lower bound and simplified the loss to a norm between predicted data and the corresponding ground truth. For segmentation, this is equivalent to predicting the segmentation mask for each time step. Compared to noise prediction, multiple studies found this mask prediction strategy to be more efficient [Fu et al., 2023, Wang et al., 2023, Lai et al., 2023]. Further, Chen et al. [2022b] suggested self-conditioning to use these predictions as additional inputs to improve diffusion models for image synthesis. Self-conditioning contains two steps: the first step predicts a noise-free sample given a noise-corrupted sample only; the second step uses the same timestep and inputs the same noise-corrupted sample as well as the prediction from the first step. This technique was later adopted for protein design [Watson et al., 2023] with an additional reverse step, where the second step performs denoising in a smaller timestep where the noise level is lower. However, in both cases, the noisy samples are directly derived from ground truth, which is not available during inference. This risks data leakage during training and empirically leads to overfitting and lack of generalisation as discussed in Chen et al. [2022a], Kolbeinsson and Mikolajczyk [2022], Lai et al. [2023]. Chen et al. [2022a], Young et al. [2022] addressed this issue by controlling the signal-to-noise ratio so that less information is preserved after noising: Chen et al. [2022a] scaled the mask value ranges to implicitly amplify the noise level, and Young et al. [2022] explicitly varied the scale and standard deviation of the Gaussian noise added to the masks. On the other hand, Kolbeinsson and Mikolajczyk [2022] proposed recursive denoising that iterates through each step during training, without using ground truth as input. However, such a strategy extends the training length by a factor of hundreds or more, making it practically infeasible for larger 3D medical image data sets. Following these studies, Fu et al. [2023] concluded that the lack of generalisation in diffusion-based segmentation models is due to the misalignment between training and inference processes. Fu et al. [2023] thus presented a two-step recycling training strategy: the first step ingests a partially noised sample for mask prediction; the predicted mask is then noise-corrupted again for denoising training. Compared to recursive denoising, this method requests a limited training time increase. This method also resembles PD-DDPM [Guo et al., 2022], where a pre-segmentation is used for noising. However, PD-DDPM requires a separate pre-segmentation network and more device memory, thus not suitable for 3D image segmentation applications.

In this work, we present a substantial extension to the preliminary work [Fu et al., 2023]. First and foremost, a novel recycling approach has been introduced. Different from Fu et al. [2023], the first step during training ingests a sample that has been completely corrupted by noise instead of a partially corrupted ground truth. This seemingly minor adjustment successfully eliminates the ground truth information from model inputs, which further aligns the training strategy towards inference. The second enhancement is the integration of a Transformer block into our network architecture. This brings our models in line with contemporary state-of-the-art approaches, rendering our findings more pertinent to real-world applications. To mitigate the increased memory consumption resulting from this addition, we employed patch-based training and inference strategies. Lastly, we extend the experiments to two more data sets, 2D

muscle ultrasound [Marzola et al., 2021] and 3D brain MR [Baid et al., 2021], to further demonstrate the robustness of the proposed method. Through extensive ablation studies across a total of four data sets, our research showcases not only the superior performance of our method in contrast to established diffusion training strategies [Ho et al., 2020, Chen et al., 2022b, Watson et al., 2023, Fu et al., 2023], but also the capacity to achieve on-par performance with non-diffusion baselines – that had not been observed in prior study [Fu et al., 2023].

### 3 Methods

#### 3.1 Denoising Diffusion Model

##### 3.1.1 Denoising Diffusion Probabilistic Model

$$\mathbf{x}_T \rightleftharpoons \cdots \rightleftharpoons \mathbf{x}_t \xrightarrow{p_{\theta}(\mathbf{x}_{t-1} \mid \mathbf{x}_t)} \mathbf{x}_{t-1} \rightleftharpoons \cdots \rightleftharpoons \mathbf{x}_0 \quad (1)$$

$$q(\mathbf{x}_t \mid \mathbf{x}_{t-1})$$

**Definition** The denoising diffusion probabilistic models (DDPM) [Ho et al., 2020] consider a *forward* process (illustrated from right to left in Equation (1)): given a sample  $\mathbf{x}_0 \sim q(\mathbf{x}_0)$ , a noise-corrupted sample  $\mathbf{x}_t$  follows a multivariate normal distribution at timestep  $t \in \{1, \dots, T\}$ ,

$$q(\mathbf{x}_t \mid \mathbf{x}_{t-1}) = \mathcal{N}(\mathbf{x}_t; \sqrt{1 - \beta_t} \mathbf{x}_{t-1}, \beta_t \mathbf{I}),$$

where  $\beta_t \in [0, 1]$ . As Gaussians are closed under convolution, given  $\mathbf{x}_0$ ,  $\mathbf{x}_t$  can be directly sampled from  $\mathbf{x}_0$  as following,

$$q(\mathbf{x}_t \mid \mathbf{x}_0) = \mathcal{N}(\mathbf{x}_t; \sqrt{\bar{\alpha}_t} \mathbf{x}_0, (1 - \bar{\alpha}_t) \mathbf{I}), \quad (2)$$

instead of performing iterative noising process which can be time-consuming and inefficient.

Correspondingly, a *reverse* process (illustrated from left to right in Equation (1)) denoises  $\mathbf{x}_t$  at each step, for  $t \in \{T, \dots, 1\}$ ,

$$p_{\theta}(\mathbf{x}_{t-1} \mid \mathbf{x}_t) = \mathcal{N}(\mathbf{x}_{t-1}; \boldsymbol{\mu}_{\theta}(\mathbf{x}_t, t), \sigma_t^2 \mathbf{I}),$$

with a predicted mean  $\boldsymbol{\mu}_{\theta}(\mathbf{x}_t, t)$  and variance  $\sigma_t^2 \mathbf{I}$ .  $\sigma_t$  is a pre-defined schedule dependent on timestep  $t$ . In this work,  $\sigma_t^2 = \tilde{\beta}_t = \frac{1 - \bar{\alpha}_{t-1}}{1 - \bar{\alpha}_t} \beta_t$  with  $\alpha_t = 1 - \beta_t$  and  $\bar{\alpha}_t = \prod_{s=0}^t \alpha_s$ .  $\boldsymbol{\mu}_{\theta}(\mathbf{x}_t, t)$  is modelled as below, also known as  $\mathbf{x}_0$  parameterisation,

$$\boldsymbol{\mu}_{\theta}(\mathbf{x}_t, t) = \frac{\sqrt{\bar{\alpha}_{t-1}} \beta_t}{1 - \bar{\alpha}_t} \hat{\mathbf{x}}_0 + \frac{1 - \bar{\alpha}_{t-1}}{1 - \bar{\alpha}_t} \sqrt{\alpha_t} \mathbf{x}_t,$$

where  $\hat{\mathbf{x}}_0$  is an estimation of  $\mathbf{x}_0$  from a learned neural network  $\hat{\mathbf{x}}_0 = f_{\theta}(\mathbf{x}_t, t)$ .

#### Training

$$\mathbf{x}_t \sim \mathcal{N}(\mathbf{x}_t; \sqrt{\bar{\alpha}_t} \mathbf{x}_0, (1 - \bar{\alpha}_t) \mathbf{I}), \quad (\text{Sampling}) \quad (3a)$$

$$\hat{\mathbf{x}}_0 = f_{\theta}(t, \mathbf{x}_t), \quad (\text{Prediction}) \quad (3b)$$

$$L_{\text{denoising}}(\theta) = \mathbb{E}_{t, \mathbf{x}_0, \mathbf{x}_t} L(\mathbf{x}_0, \hat{\mathbf{x}}_0), \quad (\text{loss calculation}) \quad (3c)$$

For each step during training, a noise corrupted sample  $\mathbf{x}_t$  is sampled and input to the neural network  $f_{\theta}$  to predict  $\mathbf{x}_0$ . The network is then trained with loss  $L_{\text{denoising}}(\theta) = \mathbb{E}_{t, \mathbf{x}_0, \mathbf{x}_t} L(\mathbf{x}_0, \hat{\mathbf{x}}_0)$  with  $t$  sampled from 1 to  $T$  and  $\epsilon_t \sim \mathcal{N}(\mathbf{0}, \mathbf{I})$ .  $L(\cdot, \cdot)$  is a loss function in the space of  $\mathbf{x}$ . In this work, importance sampling [Nichol and Dhariwal, 2021] is used for time step  $t$ , where the weight for  $t$  is proportional to  $\mathbb{E}_{\mathbf{x}_0, \mathbf{x}_t} L(\mathbf{x}_0, \hat{\mathbf{x}}_0)$ . In other words, the time steps with larger loss values are sampled more frequently.

**Inference** At inference time, the denoising starts with a randomly sampled Gaussian noise  $\mathbf{x}_T \sim \mathcal{N}(\mathbf{0}, \mathbf{I})$  and the data is denoised step-by-step for  $t = T, \dots, 1$ :

$$p_{\theta}(\mathbf{x}_{t-1} \mid \mathbf{x}_t) = \mathcal{N}(\mathbf{x}_{t-1}; \boldsymbol{\mu}_{\theta}(\mathbf{x}_t, t), \sigma_t^2 \mathbf{I})$$

$$\boldsymbol{\mu}_{\theta}(\mathbf{x}_t, t) = \frac{\sqrt{\bar{\alpha}_{t-1}} \beta_t}{1 - \bar{\alpha}_t} \hat{\mathbf{x}}_0 + \frac{1 - \bar{\alpha}_{t-1}}{1 - \bar{\alpha}_t} \sqrt{\alpha_t} \mathbf{x}_t$$

### 3.1.2 Denoising Diffusion Implicit Model

**Definition** Song et al. [2020a] parameterize  $q(\mathbf{x}_{t-1} | \mathbf{x}_t, \mathbf{x}_0)$  as follows, with  $\epsilon = \frac{\mathbf{x}_t - \sqrt{\bar{\alpha}_t} \mathbf{x}_0}{\sqrt{1 - \bar{\alpha}_t}}$ ,

$$q(\mathbf{x}_{t-1} | \mathbf{x}_t, \mathbf{x}_0) = \mathcal{N}(\mathbf{x}_{t-1}; \sqrt{\bar{\alpha}_{t-1}} \mathbf{x}_0 + \sqrt{1 - \bar{\alpha}_{t-1} - \sigma_t} \epsilon, \sigma_t^2 \mathbf{I}).$$

For any variance schedule  $\sigma_t$ , this formulation ensures  $q(\mathbf{x}_t | \mathbf{x}_0) = \mathcal{N}(\mathbf{x}_t; \sqrt{\bar{\alpha}_t} \mathbf{x}_0, (1 - \bar{\alpha}_t) \mathbf{I})$ . Particularly, if  $\sigma_t^2 = \tilde{\beta}_t$ , this represents DDPM. If  $\sigma_t = 0$  for  $t > 1$  and  $\sigma_1 = \sqrt{\tilde{\beta}_1}$ , the model is deterministic and named as denoising diffusion implicit model (DDIM).

**Inference** For DDIM, at inference time, the denoising starts with a Gaussian noise  $\mathbf{x}_T \sim \mathcal{N}(\mathbf{0}, \mathbf{I})$  and the data is denoised step-by-step for  $t = T, \dots, 1$ :

$$p_\theta(\mathbf{x}_{t-1} | \mathbf{x}_t) = \begin{cases} \mathcal{N}(\hat{\mathbf{x}}_0, \sigma_1^2 \mathbf{I}) & t = 1 \\ q(\mathbf{x}_{t-1} | \mathbf{x}_t, \mathbf{x}_{0,\theta}(\mathbf{x}_t, t)) & t > 1 \end{cases}$$

### 3.1.3 Diffusion on Segmentation Masks

In this work, noising and denoising are performed on the segmentation masks. The ground-truth binary mask, where channels correspond to classes including background, is denoted by  $\mathbf{x}_0$ . For the  $i$ -th pixel/voxel, the value for the  $j$ -th channel is in  $\{1, -1\}$ ,

$$\mathbf{x}_{0,ij} = \begin{cases} 1 & i \in \text{Class } j \\ -1 & i \in \text{Class } j \end{cases}.$$

The diffusion is therefore performed in  $[-1, 1]$  and  $\mathbf{x}$  represents a scaled probability mask. After noise corruption, the mask  $\mathbf{x}$  is clipped to  $[-1, 1]$  before being input to models.

$$\mathbf{x}_t \sim \mathcal{N}(\mathbf{x}_t; \sqrt{\bar{\alpha}_t} \mathbf{x}_0, (1 - \bar{\alpha}_t) \mathbf{I}), \quad (\text{Sampling}) \quad (4a)$$

$$\hat{\mathbf{x}}_0 = f_\theta(I, t, \mathbf{x}_t), \quad (\text{Prediction}) \quad (4b)$$

$$L_{\text{denoising}}(\theta) = \mathbb{E}_{t, \mathbf{x}_0, \mathbf{x}_t} L(\mathbf{x}_0, \hat{\mathbf{x}}_0), \quad (\text{loss calculation}) \quad (4c)$$

The training process (illustrated in Figure 1) is similar to Equation (3) apart from that segmentation network  $f_\theta(I, \mathbf{x}_t, t)$  now takes the image  $I$  as an extra input for prediction  $\hat{\mathbf{x}}_0$ .

## 3.2 Training with Recycling Strategy

At each training step, the recycling considers a sampled time step  $t < T$  and a data sample  $\mathbf{x}_0$ . First, a noise-corrupted sample  $\mathbf{x}_T$  at time step  $T$  is sampled, with  $\sqrt{\bar{\alpha}_T} \approx 0$ .  $\mathbf{x}_T$  is fed to the network  $f_\theta$  to perform a prediction  $\hat{\mathbf{x}}_0 = f_\theta(I, T, \mathbf{x}_T)$ . This prediction is then noise-corrupted to generate  $\mathbf{x}_t$ . A second prediction  $\hat{\mathbf{x}}_0 = f_\theta(I, t, \mathbf{x}_t)$  (overriding the  $\hat{\mathbf{x}}_0$  for simplicity) is produced and used for loss calculation (see Figure 1). Formally, at each timestep  $t$ , the proposed recycling (denoted as “rec.  $\mathbf{x}_T$ ”) has the following steps

$$\mathbf{x}_T \sim \mathcal{N}(\mathbf{x}_T; \sqrt{\bar{\alpha}_T} \mathbf{x}_0, (1 - \bar{\alpha}_T) \mathbf{I}), \quad (\text{rec. } \mathbf{x}_T, \text{ step 1, sampling}) \quad (5a)$$

$$\hat{\mathbf{x}}_0 = \text{StopGradient}(f_\theta(I, T, \mathbf{x}_T)), \quad (\text{rec. } \mathbf{x}_T, \text{ step 1, prediction}) \quad (5b)$$

$$\mathbf{x}_t \sim \mathcal{N}(\mathbf{x}_t; \sqrt{\bar{\alpha}_t} \hat{\mathbf{x}}_0, (1 - \bar{\alpha}_t) \mathbf{I}), \quad (\text{rec. } \mathbf{x}_T, \text{ step 2, sampling}) \quad (5c)$$

$$\hat{\mathbf{x}}_0 = f_\theta(I, t, \mathbf{x}_t), \quad (\text{rec. } \mathbf{x}_T, \text{ step 2, prediction}) \quad (5d)$$

$$L_{\text{denoising}}(\theta) = \mathbb{E}_{t, \mathbf{x}_0, \mathbf{x}_t} L(\mathbf{x}_0, \hat{\mathbf{x}}_0), \quad (\text{loss calculation}) \quad (5e)$$

In particular, stop gradient is applied to  $\hat{\mathbf{x}}_0$  in the first step to prevent the gradient calculation across two steps, in order to reduce training time. Optionally, a model with exponential moving averaged weights can be used but it requires even more memory. Compared to Equation (4), the modification of recycling only impacts the training and does not change the network architecture. It is independent of the sampling strategy during inference. Therefore, both DDPM and DDIM samplers can be used for inference.

The recycling strategy we propose in this work differs from the one introduced in Fu et al. [2023] (denoted as “rec.  $\mathbf{x}_{t+1}$ ”), illustrated in Figure 1 and the equations below,

$$\mathbf{x}_{t+1} \sim \mathcal{N}(\mathbf{x}_{t+1}; \sqrt{\bar{\alpha}_{t+1}} \mathbf{x}_0, (1 - \bar{\alpha}_{t+1}) \mathbf{I}), \quad (\text{rec. } \mathbf{x}_{t+1}, \text{ step 1, sampling}) \quad (6a)$$

$$\hat{\mathbf{x}}_0 = \text{StopGradient}(f_\theta(I, t+1, \mathbf{x}_{t+1})), \quad (\text{rec. } \mathbf{x}_{t+1}, \text{ step 1, prediction}) \quad (6b)$$

$$\mathbf{x}_t \sim \mathcal{N}(\mathbf{x}_t; \sqrt{\bar{\alpha}_t} \hat{\mathbf{x}}_0, (1 - \bar{\alpha}_t) \mathbf{I}), \quad (\text{rec. } \mathbf{x}_{t+1}, \text{ step 2, sampling}) \quad (6c)$$

$$\hat{\mathbf{x}}_0 = f_\theta(I, t, \mathbf{x}_t), \quad (\text{rec. } \mathbf{x}_{t+1}, \text{ step 2, prediction}) \quad (6d)$$

$$L_{\text{denoising}}(\theta) = \mathbb{E}_{t, \mathbf{x}_0, \mathbf{x}_t} L(\mathbf{x}_0, \hat{\mathbf{x}}_0), \quad (\text{loss calculation}) \quad (6e)$$

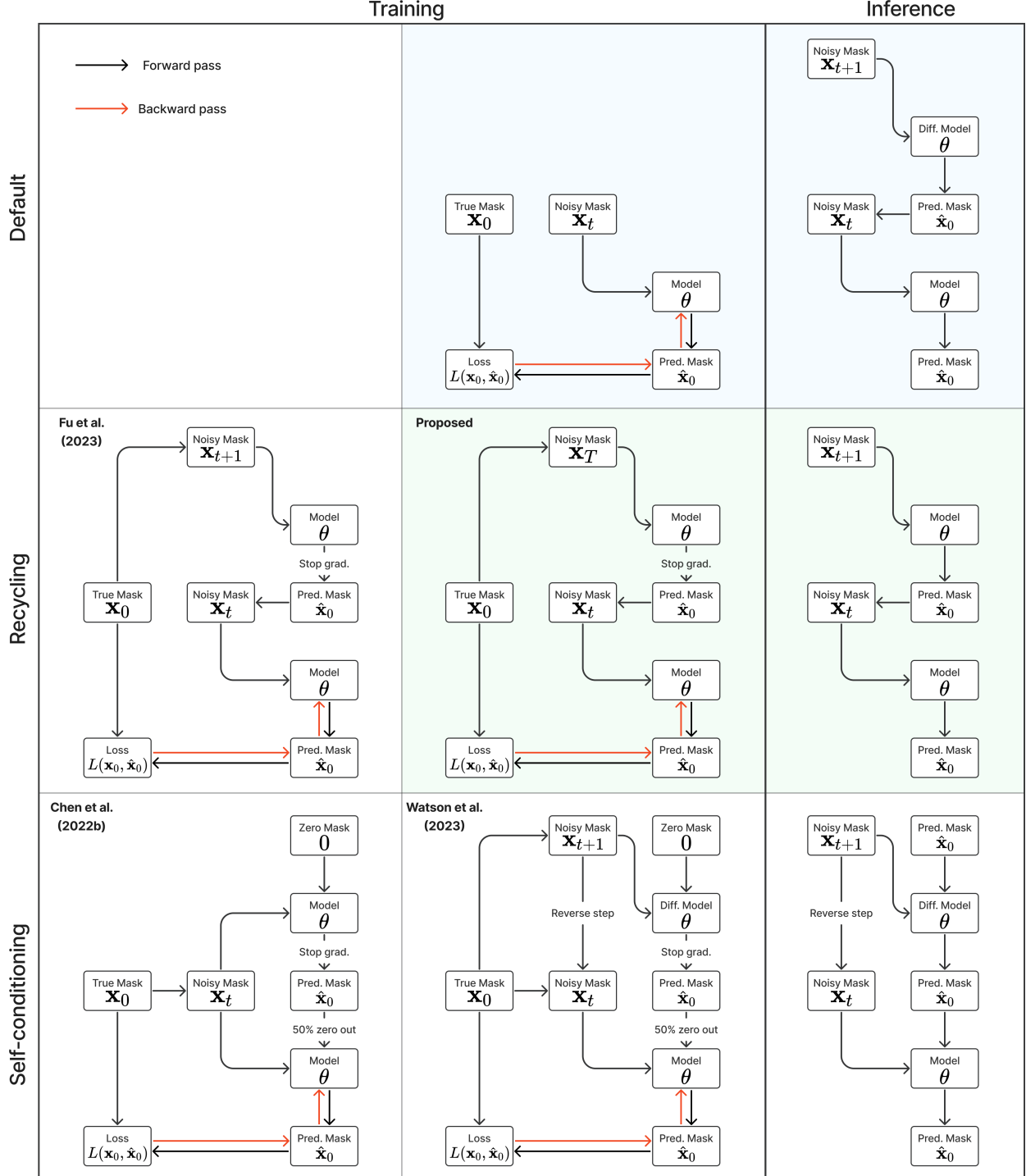


Figure 1: **Illustration of training and inference processes.** The top, middle, and bottom rows show the training and inference steps for default diffusion (highlighted in blue), diffusion with recycling, and diffusion with self-conditioning, respectively. For training, different settings are presented for recycling and self-conditioning. The proposed method is highlighted in green. Notably, recycling shares the same inference steps as default diffusion, while self-conditioning is different due to the additional input. “Pred.” and “Diff.” stands for predicted and diffusion, respectively.

In this novel approach, the first step is consistently executed at time step  $T$  instead of  $t + 1$  as shown in Equation (5). Compared to  $\mathbf{x}_{t+1}$  in Equation (6), our modification uses  $x_T$  which is fully noised and contains even less ground truth information during the initial step. This seemingly minor modification removes the ground truth information from model inputs, essentially reduce the risk of data leakage and training over-fitting. This adaptation guides the model to learn the denoising task based on its initial prediction, rather than ground truth. Consequently, the model can effectively denoise and refine the provided noisy mask, ultimately predicting the ground truth.

The recycling also differs from the self-conditioning methods proposed in Chen et al. [2022b] (denoted by “sc.  $\mathbf{x}_t$ ” in Equation (7)) and Watson et al. [2023] (denoted by “sc.  $\mathbf{x}_{t+1}$ ” in Equation (8)). Although self-conditioning also requests two forward loops during training, it differs from recycling in multiple aspects. First, the noisy samples in self-conditioning are always generated based on ground truth  $\mathbf{x}_0$  as in Equations (7a), (8a) and (8d), while the second forward step of recycling does not rely on ground truth for noisy sample generation as in Equations (5a), (5c), (6a) and (6c). Second, self-conditioning provides an additional input  $\hat{\mathbf{x}}_0$  as in Equations (7b), (7d), (8b) and (8e), while recycling does not as in Equations (5b), (5d), (6b) and (6d). Lastly, in self-conditioning  $\hat{\mathbf{x}}_0$  is replaced by zeros with 50% probabilities as in Equations (7c) and (8c), while recycling is applied constantly.

$$\mathbf{x}_t \sim \mathcal{N}(\mathbf{x}_t; \sqrt{\bar{\alpha}_t} \mathbf{x}_0, (1 - \bar{\alpha}_t) \mathbf{I}), \quad (\text{sc. } \mathbf{x}_t, \text{ step 1, sampling}) \quad (7a)$$

$$\hat{\mathbf{x}}_0 = \text{StopGradient}(f_\theta(I, t, \mathbf{x}_t, \mathbf{0})), \quad (\text{sc. } \mathbf{x}_t, \text{ step 1, prediction}) \quad (7b)$$

$$\hat{\mathbf{x}}_0 = \text{Dropout}_{p=50\%}(\hat{\mathbf{x}}_0), \quad (\text{sc. } \mathbf{x}_t, \text{ step 2, dropout}) \quad (7c)$$

$$\hat{\mathbf{x}}_0 = f_\theta(I, t, \mathbf{x}_t, \hat{\mathbf{x}}_0), \quad (\text{sc. } \mathbf{x}_t, \text{ step 2, prediction}) \quad (7d)$$

$$L_{\text{denoising}}(\theta) = \mathbb{E}_{t, \mathbf{x}_0, \mathbf{x}_t} L(\mathbf{x}_0, \hat{\mathbf{x}}_0), \quad (\text{loss calculation}) \quad (7e)$$

$$\mathbf{x}_{t+1} \sim \mathcal{N}(\mathbf{x}_{t+1}; \sqrt{\bar{\alpha}_{t+1}} \mathbf{x}_0, (1 - \bar{\alpha}_{t+1}) \mathbf{I}), \quad (\text{sc. } \mathbf{x}_{t+1}, \text{ step 1, sampling}) \quad (8a)$$

$$\hat{\mathbf{x}}_0 = \text{StopGradient}(f_\theta(I, t + 1, \mathbf{x}_{t+1}, \mathbf{0})), \quad (\text{sc. } \mathbf{x}_{t+1}, \text{ step 1, prediction}) \quad (8b)$$

$$\hat{\mathbf{x}}_0 = \text{Dropout}_{p=50\%}(\hat{\mathbf{x}}_0), \quad (\text{sc. } \mathbf{x}_{t+1}, \text{ step 2, dropout}) \quad (8c)$$

$$\mathbf{x}_t \sim \mathcal{N}(\mathbf{x}_t; \tilde{\mu}, \tilde{\beta}_{t+1} \mathbf{I}), \quad (\text{sc. } \mathbf{x}_{t+1}, \text{ step 2, sampling}) \quad (8d)$$

$$\tilde{\mu} = \frac{\sqrt{\bar{\alpha}_t} \beta_{t+1}}{1 - \bar{\alpha}_{t+1}} \mathbf{x}_0 + \frac{1 - \bar{\alpha}_t}{1 - \bar{\alpha}_{t+1}} \sqrt{\alpha_{t+1}} \mathbf{x}_{t+1}$$

$$\hat{\mathbf{x}}_0 = f_\theta(I, t, \mathbf{x}_t, \hat{\mathbf{x}}_0), \quad (\text{sc. } \mathbf{x}_{t+1}, \text{ step 2, prediction}) \quad (8e)$$

$$L_{\text{denoising}}(\theta) = \mathbb{E}_{t, \mathbf{x}_0, \mathbf{x}_t} L(\mathbf{x}_0, \hat{\mathbf{x}}_0), \quad (\text{loss calculation}) \quad (8f)$$

## 4 Experiment Setting

### 4.1 Data

#### 4.1.1 Muscle Ultrasound

The data set<sup>1</sup> [Marzola et al., 2021] (denoted by Muscle US) provides 3910 labelled transverse musculoskeletal ultrasound images, which have been split into 2531, 666, and 713 images for training, validation, and test sets, respectively. Images have shape  $480 \times 512$ . The predicted masks were post-processed, following Marzola et al. [2021]. After filling the holes, multiple morphological operations were performed, including an erosion with a disk of radius 3 pixels, a dilation with a disk of radius 5 pixels, and an opening with a disk of radius 10 pixels. Afterwards, only the largest connected component is preserved if the second-largest structure was smaller than 75% of the largest one; otherwise, the most superficial (i.e., towards the top of the image) one between the two largest components is preserved. Finally, holes were filled if there were any.

#### 4.1.2 Abdominal CT (AMOS)

The data set<sup>2</sup> [Ji et al., 2022] provides 200 and 100 CT image-mask pairs for 15 abdominal organs in training and validation sets. The validation set was randomly split into non-overlapping validation and test sets, with 10 and 90 images, respectively. Images were firstly resampled with a voxel dimension of  $1.5 \times 1.5 \times 5.0$  (mm). HU values were clipped to  $[-991, 362]$  and images were normalised so that the intensity has zero mean and unit variance. Lastly, images were centre-cropped to shape  $192 \times 128 \times 128$ . During training the patch size is  $128 \times 128 \times 128$ . During inference, the overlap between patches is  $64 \times 0 \times 0$ , and the predictions on the overlap are averaged.

<sup>1</sup><https://data.mendeley.com/datasets/3jy7wz8d/1>

<sup>2</sup><https://zenodo.org/record/7155725#.ZAkbe-zP2r0>

### 4.1.3 Prostate MR

The data set<sup>3</sup> [Li et al., 2022b] contains 589 T2-weighted image-mask pairs for 8 anatomical structures from 7 institutions. The images were randomly split into non-overlapping training, validation, and test sets, with 411, 14, and 164 images in each split, respectively. The validation split has two images from each institution. Images were resampled with a voxel dimension of  $0.75 \times 0.75 \times 2.5$  (mm). Afterwards, images were normalised so that the intensity has zero mean and unit variance. Lastly, images were centre-cropped to shape  $256 \times 256 \times 48$ . During training the patch size is  $256 \times 256 \times 32$ . During inference, the overlap between patches is  $0 \times 0 \times 16$ , and the predictions on the overlap are averaged.

### 4.1.4 Brain MR (BraTS 2021)

The data set<sup>4</sup> [Baid et al., 2021] provides 1251MR segmented mpMRI scans for brain tumour. The data set was randomly split into non-overlapping training, validation and test sets, with 938, 31, and 282 samples, respectively. The whole tumour mask is generated as foreground class, including GD-enhancing tumour, the peritumoral edematous/invasive tissue, and the necrotic tumour core. The task is therefore a binary segmentation. Four modalities are available, including T1-weighted (T1), post-contrast T1-weighted (T1Gd), T2-weighted (T2), and T2 Fluid Attenuated Inversion Recovery (T2-FLAIR). Voxel dimension is  $1.0 \times 1.0 \times 1.0$  (mm). Images were firstly normalised so that the intensity has zero mean and unit variance. Lastly, images were centre-cropped to shape  $179 \times 219 \times 155$  to remove the common background. During training the patch size is  $128 \times 128 \times 128$ . During inference, the overlap between patches is  $77 \times 37 \times 101$ , and the predictions on the overlap are averaged.

## 4.2 Implementation Details

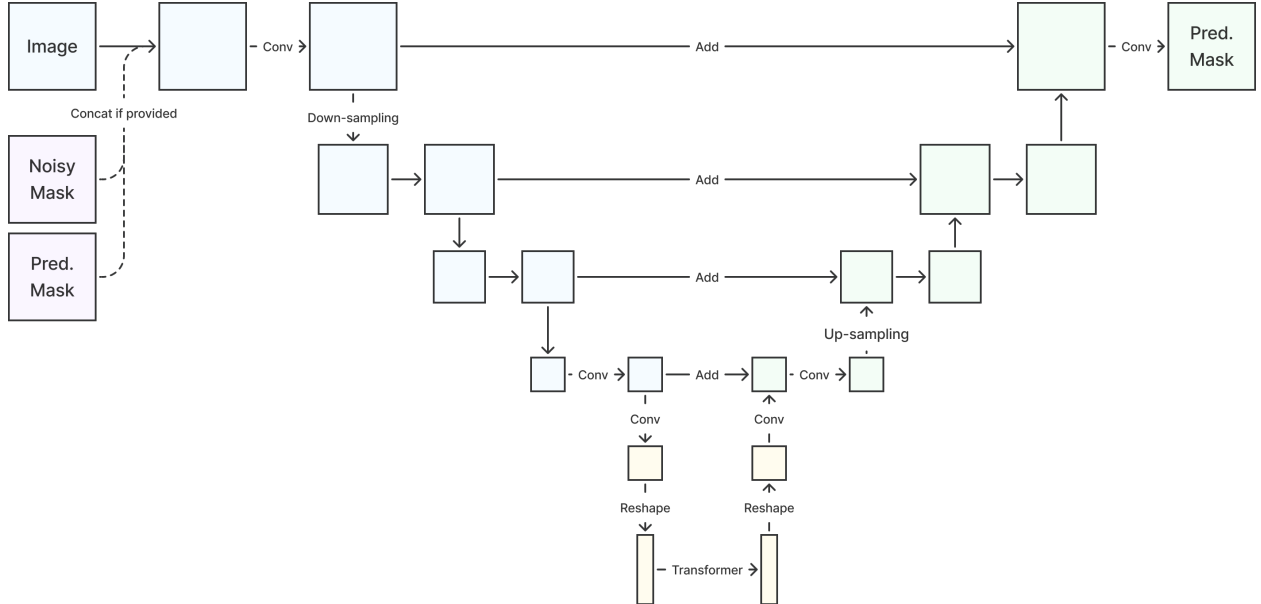


Figure 2: **Unet architecture for diffusion and non-diffusion models.** The inputs are concatenated when noisy mask (from diffusion models) or predicted mask (from self-conditioning) is provided. The tensor is enriched with convolution (time-conditioned for diffusion models) and down-sampling layers, then passed into a Transformer with positional encoding, the output is then enriched with convolution and up-sampling layers, and finally, prediction is performed with an additional  $1 \times 1$  convolutional layer. “Pred.” stands for predicted.

2D and 3D U-net variants with attention mechanisms were used for benchmarking the reference performance from cross-data-set non-diffusion models. The architecture is illustrated in Figure 2. U-nets have four layers with 32, 64, 128, and 256 channels, respectively. For diffusion-based models, noise-corrupted masks were concatenated. Time was encoded using sinusoidal positional embedding [Rombach et al., 2022] and used in convolution layers.

<sup>3</sup><https://zenodo.org/record/7013610#.ZAkaxuzP2rM>

<sup>4</sup><https://www.kaggle.com/datasets/dschettler8845/brats-2021-task1>

For denoising training, a linear  $\beta$  schedule between 0.0001 and 0.02 was used for  $T = 1001$ . The segmentation-specific loss function is by default cross-entropy and foreground-only Dice loss, with weight 20 and 1 respectively [Kirillov et al., 2023]. Random rotation, translation and scaling were adopted for data augmentation during training. Training hyper-parameters are listed in Table 7. Hyper-parameter were configured empirically without extensive tuning.

Models were trained once and checkpoints were saved every 500 steps. The checkpoint having the best mean binary Dice score (without background class) on the validation set was used for testing. For DDIM, the training was the same as DDPM while both validation and testing were performed using DDIM. Experiments were performed using bfloat16 mixed precision on TPU v3-8, which has  $16 \times 8$  GB device memory. However, each device has only 16 GB memory, meaning that the model and data have to fit into 16 GB memory. The JAX-based framework has been released on <https://github.com/mathpluscode/ImgX-DiffSeg>.

The mean binary Dice score (DS) and 95% Hausdorff distance (HD), averaged over foreground classes, were reported for the test sets. Dice score is reported in percentage, between 0% and 100%. For Hausdorff distance, values are in mm for 3D volumes and pixels for 2D images. Paired Student’s t-tests with a significance level of  $\alpha = 0.01$  were performed on Dice score to test statistical significance between model performance.

## 5 Results and Discussion

### 5.1 Diffusion Training Strategy Comparison

We compared the diffusion models trained using the suggested recycling approach (diff. rec.  $\mathbf{x}_T$ ) against various benchmarks. These included the baseline standard diffusion models (diff.), those utilizing self-conditioning techniques from Chen et al. [2022b] (diff. sc.  $\mathbf{x}_t$ ) and Watson et al. [2023] (diff. sc.  $\mathbf{x}_{t+1}$ ), and also the recycling method from Fu et al. [2023] (diff. rec.  $\mathbf{x}_{t+1}$ ), as specified in Table 1. Both DDPM and DDIM samplers were evaluated using each training strategy. All results were reported on the holdout test splits.

Our proposed recycling method achieved mean Dice scores of 88.23%, 87.45%, 85.54%, and 92.29% on muscle ultrasound, abdominal CT, prostate MR, and brain MR data sets, respectively. These scores marked absolute improvements of 1.63%, 2.20%, 1.93%, and 2.00% over standard diffusion models, respectively. The relative improvements are 1.88%, 2.58%, 2.31%, and 2.22% correspondingly. Impressively, this novel strategy consistently outperformed the other three training approaches in terms of both Dice score and Hausdorff distance. The observed differences were significant for all data sets in terms of Dice score. These findings held true for both DDPM and DDIM samplers, underscoring the robustness and wide applicability of the proposed training strategy.

For unconditional image synthesis, diffusion models begin without any initial information. In the case of text-conditioned image synthesis, diffusion models possess partial information, however, the text often only provides high-level context instead of pixel- or voxel-wise information. In contrast to these situations, the application of diffusion models for segmentation is distinctive in that all the necessary information is already supplied by the input image. The strength of diffusion models lies in their capacity to iteratively refine predictions, coupled with their inherent generative nature. Nonetheless, as depicted in Figure 3, standard diffusion models often yield segmentation masks at the last step that are less accurate than the initial prediction. Similar challenges are observed with self-conditioning strategies and previously proposed recycling methods. The newly introduced recycling method is the only approach that enhances initial segmentation predictions for more than half of the test images. Moreover, the average performance per step has been visualised in Figure 4, where diffusion models frequently exhibit gradually declining or unstable performance during inference, in terms of both Dice score and Hausdorff distance. It’s interesting to observe that often, the optimal prediction emerges not at the final step but rather at an intermediate stage. This has been observed in all diffusion models except the newly proposed diffusion model with the innovative recycling method. In the latter case, the quality of segmentation consistently improves or remains stable throughout the inference process, setting it apart from the observed trend. A qualitative comparison on an example muscle ultrasound image has been illustrated in Figure 5, where the proposed diffusion model was able to refine the segmentation mask progressively. Similar observations have been noted with DDIM sampler as well, as shown in Figure 8 and Figure 9. This finding aligns with the discussions from Kolbeinsson and Mikolajczyk [2022], Lai et al. [2023] that the diffusion-based segmentation model performance is strongly influenced by the prediction of the initial step. For self-conditioning or the previously proposed recycling, the denoising training relies on the ground truth to varying degrees therefore the diffusion models are trained with ground truth like initial predictions. However, no ground truth is available during inference and the distributions of initial predictions from the trained models are dissimilar from ground truths. This results in an out-of-sample inference and therefore declining performance. In contrast, the proposed method ingests model predictions for both the training and inference phases without the bias towards ground truth. These observations reaffirm the importance and benefits of harmonizing the training and inference processes. This alignment is crucial to mitigate data leakage, prevent overfitting, and help generalisation.

Table 1: **Diffusion training strategies comparison.** “Diff.” represents standard diffusion. “sc.  $\mathbf{x}_t$ ” and “sc.  $\mathbf{x}_{t+1}$ ” represents self-conditioning from Chen et al. [2022b] and Watson et al. [2023], respectively. “rec.  $\mathbf{x}_{t+1}$ ” and “rec.  $\mathbf{x}_T$ ” represents recycling from Fu et al. [2023] and the proposed recycling in this work, respectively. The best results are underlined and a wavy line indicates the difference to the second best is significant with p-value  $< 0.01$ .

Method	DDPM		DDIM	
	DS $\uparrow$	HD $\downarrow$	DS $\uparrow$	HD $\downarrow$
Diff.	86.60 $\pm$ 12.38	41.11 $\pm$ 35.48	86.18 $\pm$ 12.41	42.31 $\pm$ 35.82
Diff. sc. $\mathbf{x}_t$	86.35 $\pm$ 14.14	40.42 $\pm$ 37.53	85.96 $\pm$ 13.78	42.00 $\pm$ 36.76
Diff. sc. $\mathbf{x}_{t+1}$	87.14 $\pm$ 11.48	39.24 $\pm$ 32.83	86.30 $\pm$ 11.49	41.89 $\pm$ 32.72
Diff. rec. $\mathbf{x}_{t+1}$	87.44 $\pm$ 12.39	39.68 $\pm$ 36.21	87.43 $\pm$ 12.25	39.82 $\pm$ 35.39
Diff. rec. $\mathbf{x}_T$	<u>88.23 <math>\pm</math> 11.69</u>	<u>35.37 <math>\pm</math> 31.79</u>	<u>88.21 <math>\pm</math> 11.70</u>	<u>35.52 <math>\pm</math> 31.91</u>

(a) Muscle Ultrasound

Method	DDPM		DDIM	
	DS $\uparrow$	HD $\downarrow$	DS $\uparrow$	HD $\downarrow$
Diff.	85.25 $\pm$ 5.36	7.12 $\pm$ 3.83	85.59 $\pm$ 5.24	7.13 $\pm$ 3.98
Diff. sc. $\mathbf{x}_t$	86.04 $\pm$ 5.12	7.06 $\pm$ 4.20	85.50 $\pm$ 5.14	7.21 $\pm$ 4.16
Diff. sc. $\mathbf{x}_{t+1}$	85.86 $\pm$ 5.27	6.98 $\pm$ 3.54	85.25 $\pm$ 5.42	7.28 $\pm$ 3.72
Diff. rec. $\mathbf{x}_{t+1}$	86.48 $\pm$ 5.24	6.69 $\pm$ 4.59	86.35 $\pm$ 5.31	6.75 $\pm$ 4.55
Diff. rec. $\mathbf{x}_T$	<u>87.45 <math>\pm</math> 5.43</u>	<u>6.56 <math>\pm</math> 5.44</u>	<u>87.45 <math>\pm</math> 5.43</u>	<u>6.55 <math>\pm</math> 5.43</u>

(b) Abdominal CT

Method	DDPM		DDIM	
	DS $\uparrow$	HD $\downarrow$	DS $\uparrow$	HD $\downarrow$
Diff.	83.61 $\pm$ 4.87	5.10 $\pm$ 2.40	83.11 $\pm$ 4.81	5.00 $\pm$ 2.35
Diff. sc. $\mathbf{x}_t$	83.47 $\pm$ 4.85	5.17 $\pm$ 2.65	82.49 $\pm$ 4.88	5.42 $\pm$ 2.70
Diff. sc. $\mathbf{x}_{t+1}$	83.97 $\pm$ 4.85	4.93 $\pm$ 2.66	83.00 $\pm$ 4.89	5.10 $\pm$ 2.64
Diff. rec. $\mathbf{x}_{t+1}$	84.29 $\pm$ 5.12	4.59 $\pm$ 2.21	84.21 $\pm$ 4.89	4.96 $\pm$ 2.92
Diff. rec. $\mathbf{x}_T$	<u>85.54 <math>\pm</math> 5.20</u>	<u>4.40 <math>\pm</math> 1.96</u>	<u>85.54 <math>\pm</math> 5.20</u>	<u>4.41 <math>\pm</math> 1.96</u>

(c) Prostate MR

Method	DDPM		DDIM	
	DS $\uparrow$	HD $\downarrow$	DS $\uparrow$	HD $\downarrow$
Diff.	90.29 $\pm$ 12.98	8.46 $\pm$ 15.55	89.94 $\pm$ 13.00	8.55 $\pm$ 15.50
Diff. sc. $\mathbf{x}_t$	90.12 $\pm$ 12.39	9.55 $\pm$ 17.18	89.73 $\pm$ 12.61	9.67 $\pm$ 16.86
Diff. sc. $\mathbf{x}_{t+1}$	89.11 $\pm$ 14.70	9.63 $\pm$ 17.47	88.75 $\pm$ 14.77	9.62 $\pm$ 16.97
Diff. rec. $\mathbf{x}_{t+1}$	86.97 $\pm$ 10.94	9.83 $\pm$ 12.62	84.76 $\pm$ 13.42	12.52 $\pm$ 15.55
Diff. rec. $\mathbf{x}_T$	<u>92.29 <math>\pm</math> 8.55</u>	<u>7.03 <math>\pm</math> 13.48</u>	<u>92.29 <math>\pm</math> 8.55</u>	<u>7.03 <math>\pm</math> 13.48</u>

(d) Brain MR

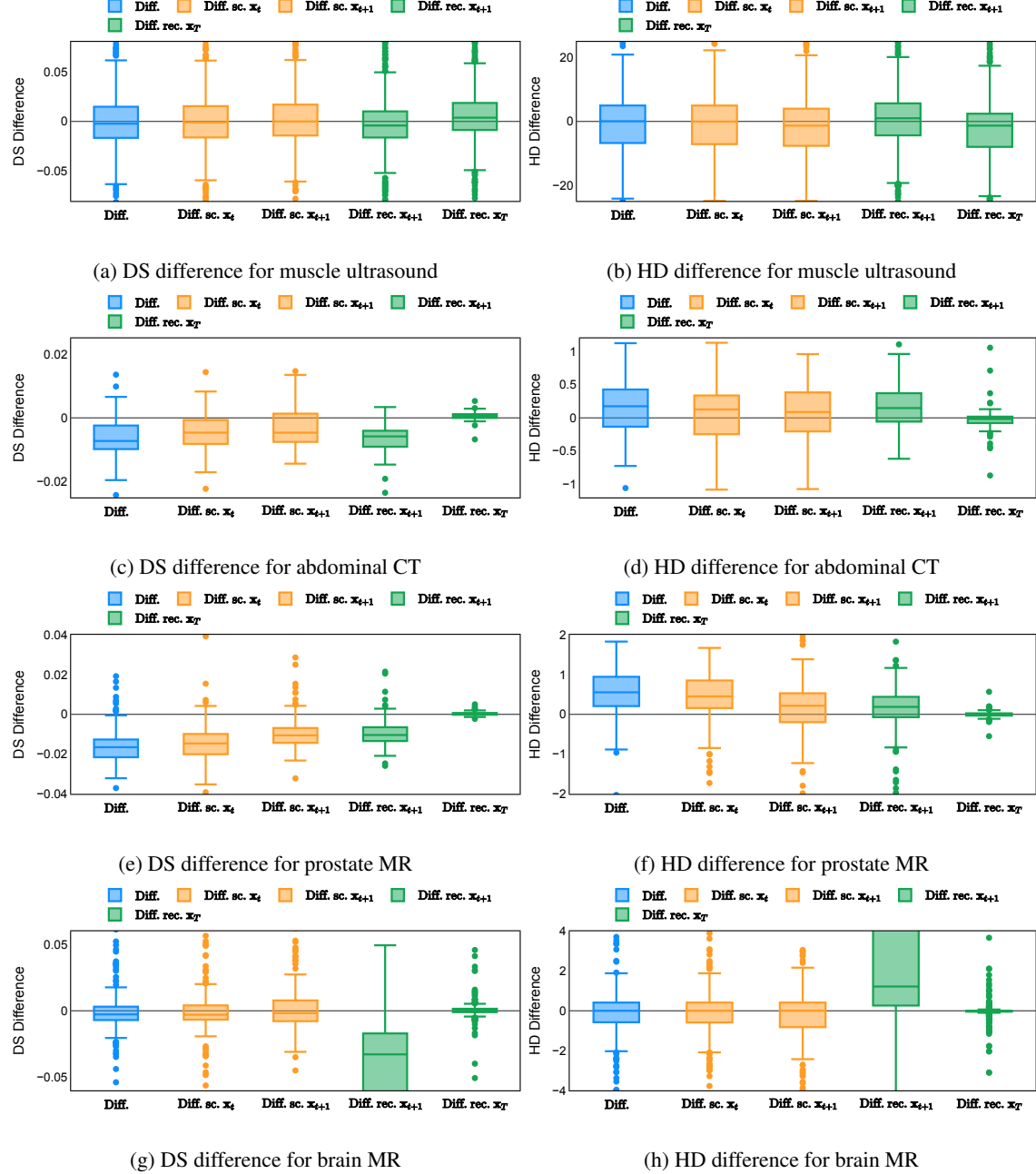


Figure 3: **Segmentation performance difference between the last step and first step.** “Diff.” represents standard diffusion. “sc.  $x_t$ ” and “sc.  $x_{t+1}$ ” represents self-conditioning from Chen et al. [2022b] and Watson et al. [2023], respectively. “rec.  $x_{t+1}$ ” and “rec.  $x_T$ ” represents recycling from Fu et al. [2023] and the proposed recycling in this work, respectively. The sampler is DDPM. DS and HD represents Dice score and Hausdorff distance, respectively. The difference is the value at the last step subtracted by the one at the first step. A positive value for Dice score difference or a negative value for Hausdorff distance means improvement.

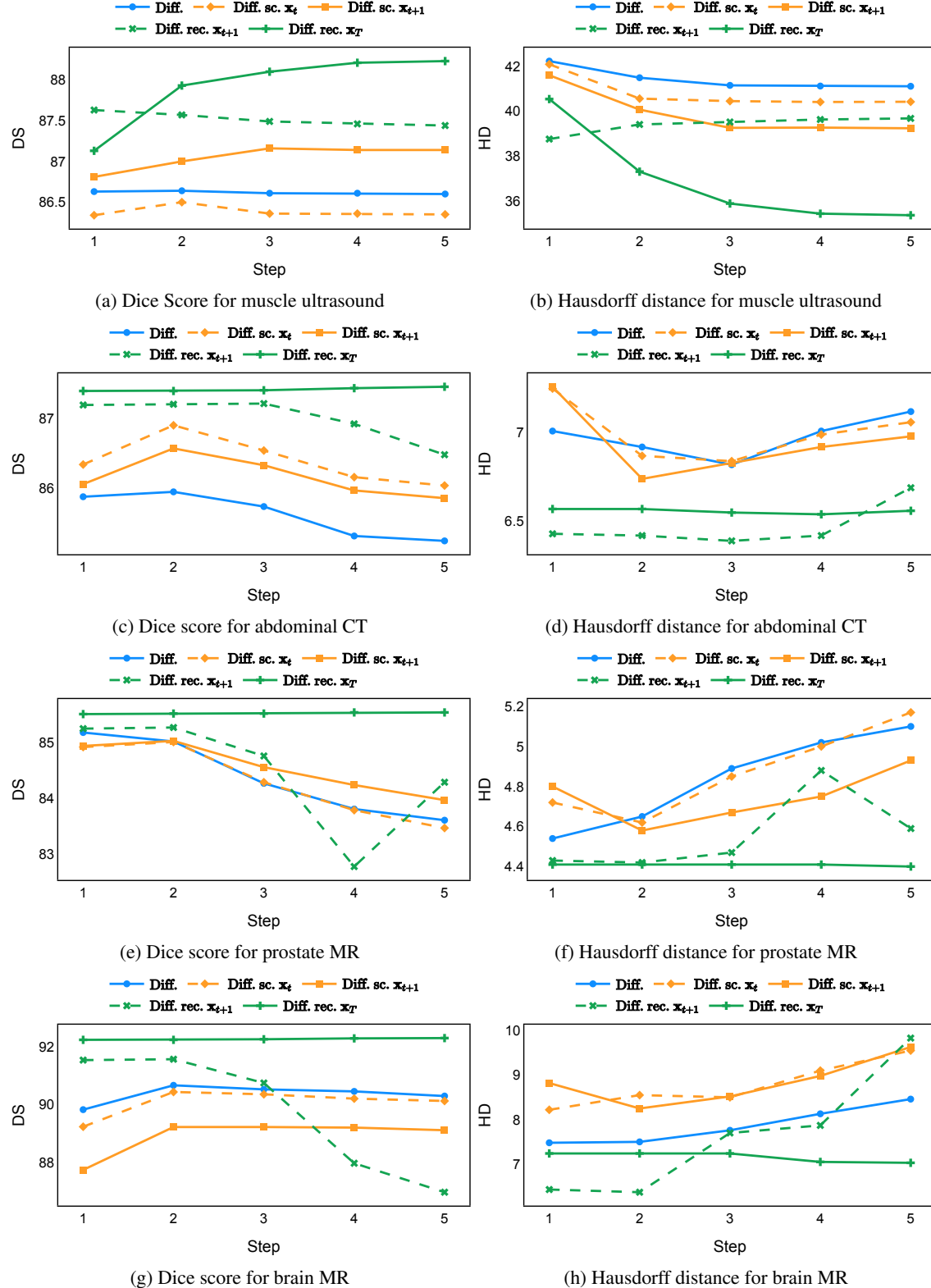


Figure 4: **Segmentation performance per step.** “Diff.” represents standard diffusion. “sc.  $x_t$ ” and “sc.  $x_{t+1}$ ” represents self-conditioning from Chen et al. [2022b] and Watson et al. [2023], respectively. “rec.  $x_{t+1}$ ” and “rec.  $x_T$ ” represents recycling from Fu et al. [2023] and the proposed recycling in this work, respectively. The sampler is DDPM.

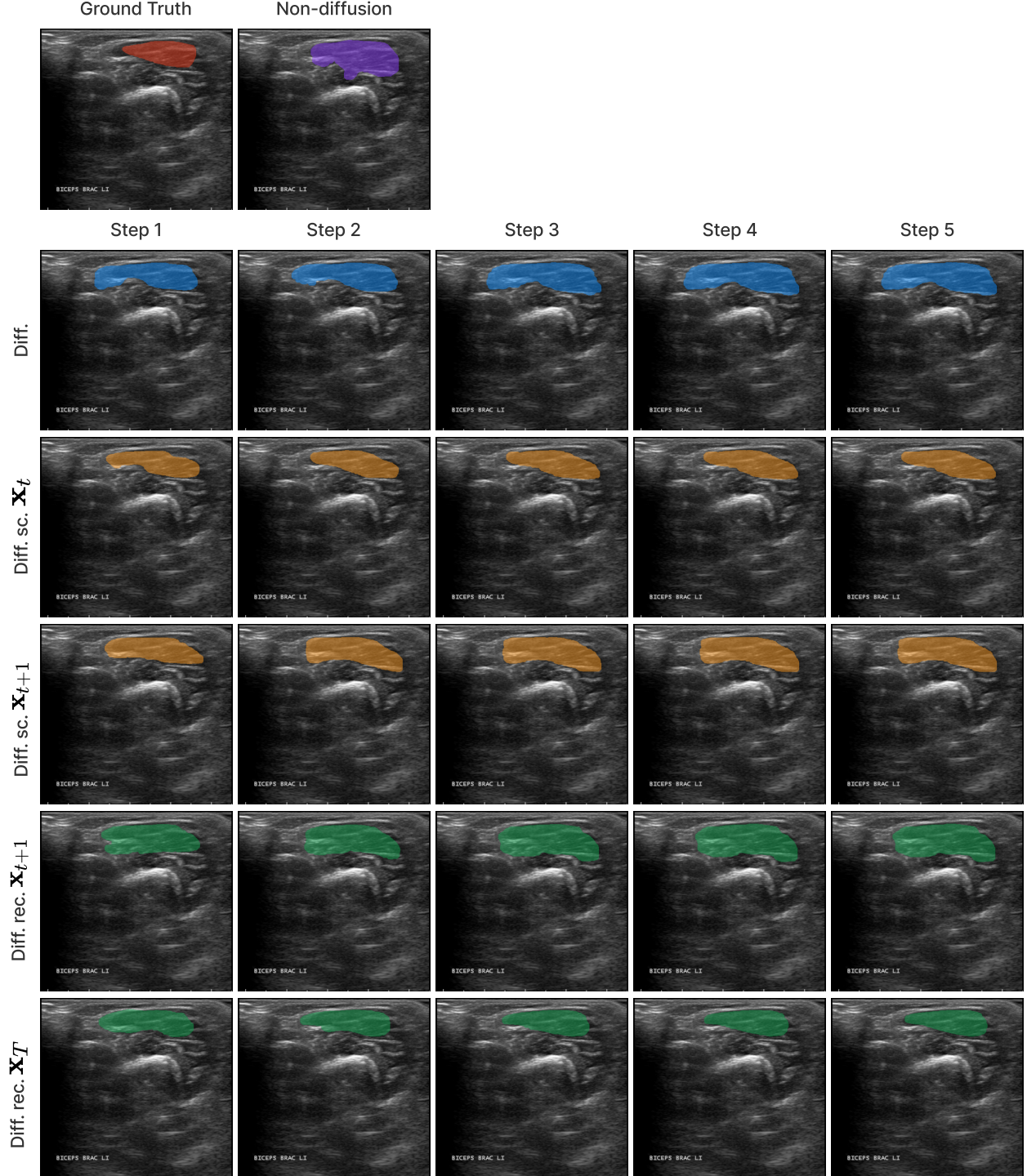


Figure 5: **Diffusion training strategies comparison on muscle ultrasound example.** “Diff.” represents standard diffusion. “sc.  $x_t$ ” and “sc.  $x_{t+1}$ ” represents self-conditioning from Chen et al. [2022b] and Watson et al. [2023], respectively. “rec.  $x_{t+1}$ ” and “rec.  $x_T$ ” represents recycling from Fu et al. [2023] and the proposed recycling in this work, respectively. While different diffusion models has similar performance on the first step, the proposed method (last row) is able to refine the segmentation mask.

It's worth noting that Fu et al. [2023] recommended incorporating a shortened variance schedule during training, mirroring that used during inference, in addition to the recycling technique. This modification resulted in enhanced performance for every training strategy on the muscle ultrasound data set (as detailed in Table 8a). However, this adaptation only yielded enhancements for certain training strategies in the abdominal CT data set (as depicted in Table 8b). Moreover, not all differences observed are statistically significant. This suggests that the advantage of the modified training variance schedule may be application-dependent and sensitive to the change of model architectures and hyper-parameters. The variance schedule in our study therefore remains unchanged, maintained at 1001 steps.

## 5.2 Ablation Studies

Table 2: **Diffusion with different number of sampling steps.** Sampler is DDPM. Diffusion models were trained using the proposed recycling method (Diff. rec.  $x_T$ ). OOM indicates that out of memory errors were encountered.

Data Set	# Sampling Steps	Dice Score	Hausdorff Distance
Muscle ultrasound	2	$88.01 \pm 12.07$	$36.55 \pm 32.66$
	5	$88.23 \pm 11.69$	$35.37 \pm 31.79$
	11	$88.30 \pm 11.29$	$35.25 \pm 30.64$
Abdominal CT	2	$87.44 \pm 5.43$	$6.56 \pm 5.42$
	5	$87.45 \pm 5.43$	$6.56 \pm 5.44$
	11	OOM	OOM
Prostate MR	2	$85.54 \pm 5.19$	$4.40 \pm 1.96$
	5	$85.54 \pm 5.20$	$4.40 \pm 1.96$
	11	$85.54 \pm 5.20$	$4.40 \pm 1.96$
Brain MR	2	$92.29 \pm 8.54$	$7.03 \pm 13.47$
	5	$92.29 \pm 8.55$	$7.03 \pm 13.48$
	11	$92.29 \pm 8.57$	$7.02 \pm 13.48$

Table 3: **Diffusion model performance across different inference seeds.** For each sample, the maximum difference ( $\Delta$ ) across five random seeds is calculated. The average across all samples is reported.

Data Set	Mean $\Delta$ Dice Score				
	Step 1	Step 2	Step 3	Step 4	Step 5
Muscle ultrasound	0.0212	0.0165	0.0122	0.0081	0.0051
Abdominal CT	0.0009	0.0010	0.0009	0.0008	0.0004
Prostate MR	0.0004	0.0004	0.0004	0.0004	0.0002
Brain MR	0.0005	0.0005	0.0005	0.0003	0.0001

Data Set	Mean $\Delta$ Hausdorff Distance				
	Step 1	Step 2	Step 3	Step 4	Step 5
Muscle ultrasound	10.0582	7.0020	4.7440	3.1758	1.8164
Abdominal CT	0.1481	0.1339	0.1221	0.0751	0.0673
Prostate MR	0.0447	0.0426	0.0499	0.0431	0.0209
Brain MR	0.0758	0.0779	0.0678	0.0616	0.0197

Diffusion models were trained using a thousand steps, yet employing the same number of steps for inference can be cost-prohibitive, particularly for processing 3D image volumes. As a result, practical inference commonly utilises a condensed schedule with a limited number of steps. While this approach reduces computational expenses, the resulting sample quality might be compromised. An ablation study of the numbers of timesteps during inference has therefore been performed across data sets with the proposed recycling-based diffusion model. DDPM sampler was used. The results have been summarised in Table 2. Notably, increasing the number of steps yielded improved performance for the muscle ultrasound dataset, as indicated by enhanced Dice scores and reduced Hausdorff distances. However, the observed differences were not statistically significant ( $p > 0.01$ ), with the exception of the Hausdorff distance improvement achieved with an increase to five steps ( $p = 0.004$ ). For prostate MR and brain MR data sets, the models remained almost the same performance regardless of the inference length ( $p > 0.1$ ). Given that longer inference times and increased device memory usage are associated with more timesteps (e.g. out-of-memory errors were encountered

with Abdominal CT at 11 steps), the trade-off between computational resources and performance suggests that a five-step sampling schedule provides the optimal balance.

Different from deterministic models, the inference process of the diffusion model inherently incorporates stochasticity and models a distribution of the segmentation masks. Using the DDPM sampler with the proposed recycling-based diffusion model, the inference on each data set has been repeated with five different random seeds. Consequently, each sample has five distinct predicted masks. The maximum differences across five predictions are computed for the Dice score and Hausdorff distance, denoted by  $\Delta$  Dice score and  $\Delta$  Hausdorff distance, respectively. The average of this performance difference across all samples in the test set has been reported in Table 3 for all data sets. While the magnitude of the average difference (mean  $\Delta$ ) varies across data sets, a common trend was observed where mean  $\Delta$  diminished during the sampling process for both metrics. In other words, despite different initial predictions, the model’s predictions gradually converge as the difference across seeds decreases. Moreover, the relative magnitude of the mean  $\Delta$  Hausdorff distance (e.g. 1.82 at the last step for muscle ultrasound represents around 5% fluctuation compared to 35.37, the mean Hausdorff distance to ground truth) is larger than the relative magnitude for Dice score (e.g. 0.0051 at the last step for muscle ultrasound is around 0.006% fluctuation compared to 88.23 the mean Hausdorff distance to ground truth). We hypothesise that the variation among predictions may predominantly revolve around local refinements in mask boundaries, as opposed to significant alterations like expansion or contraction of foreground areas. This may open a direction for further improving diffusion training: instead of performing independent noising per pixel/voxel results in fragmented and disjointed masks, the noising can be morphology-informed such that the noise-corrupted masks expand or contract the foreground with continuous boundaries.

### 5.3 Comparison to Non-diffusion Models

Table 4: **Segmentation performance comparison to non-diffusion models.** “No diff.” represents non-diffusion model. “Diff. rec.  $\mathbf{x}_T$ ” represents the diffusion model with proposed recycling. The inference sampler is DDPM. The best results are underlined and a wavy line indicates the difference is significant with  $p\text{-value} < 0.01$ .

Data Set	Method	DS $\uparrow$	p-value	HD $\downarrow$	p-value
Muscle ultrasound	Diff. rec. $\mathbf{x}_T$	$88.23 \pm 11.69$	0.777	$35.37 \pm 31.79$	0.131
	No diff.	$88.15 \pm 10.77$		$36.86 \pm 30.04$	
Abdominal CT	Diff. rec. $\mathbf{x}_T$	$87.45 \pm 5.43$	0.353	$6.56 \pm 5.44$	0.672
	No diff.	$87.59 \pm 5.10$		$6.36 \pm 3.86$	
Prostate MR	Diff. rec. $\mathbf{x}_T$	$85.54 \pm 5.20$	0.001	$4.40 \pm 1.96$	0.050
	No diff.	$85.22 \pm 5.18$		$4.62 \pm 2.37$	
Brain MR	Diff. rec. $\mathbf{x}_T$	$92.29 \pm 8.55$	0.001	$7.03 \pm 13.48$	0.050
	No diff.	$92.43 \pm 9.10$		$5.20 \pm 9.56$	

The proposed diffusion models (“Diff. rec.  $\mathbf{x}_T$ ”) were compared with their non-diffusion counterparts (“No diff.”), where models with identical architectures were trained under the same scheme with the same compute budget. This provides a fair comparison without application-specific adjustments. Details of the implementation have been described in Section 4.2 or can be found in the repository <https://github.com/mathpluscode/ImgX-DiffSeg>. For diffusion models, the performance with DDPM was selected. As shown in Table 4, The diffusion models yielded similar performance across all data sets. The difference is not significant for muscle ultrasound and abdominal CT, but significant for prostate MR and brain MR in terms of Dice score. The Hausdorff distance difference is however not significant for all data sets. Furthermore, Figure 7 directly compares the performance of two methods on the tested samples. In fact, the proposed diffusion model achieved better performance on more than 50% samples for muscle ultrasound, abdominal CT and prostate MR data sets.

Abdominal CT and prostate MR are two data sets with multiple classes and their per-class segmentation performances are summarised in Table 5 and Table 6, respectively. Upon comparing diffusion models and non-diffusion models, neither consistently outperformed the other across all classes (see Figure 6 for the segmentation error visualised in 3D). This implies that challenges persist in employing diffusion models for image segmentation to significantly elevate performance within the same compute budget. To the best of our knowledge, this is the first time that diffusion models achieved comparable performance against standard non-diffusion-based models with the same architecture and compute budget.

We highlight that the value of the competitive performance from alternative methods, in particular a different class of generative model-based approaches, is beyond the replacement of current segmentation algorithms for specific potential

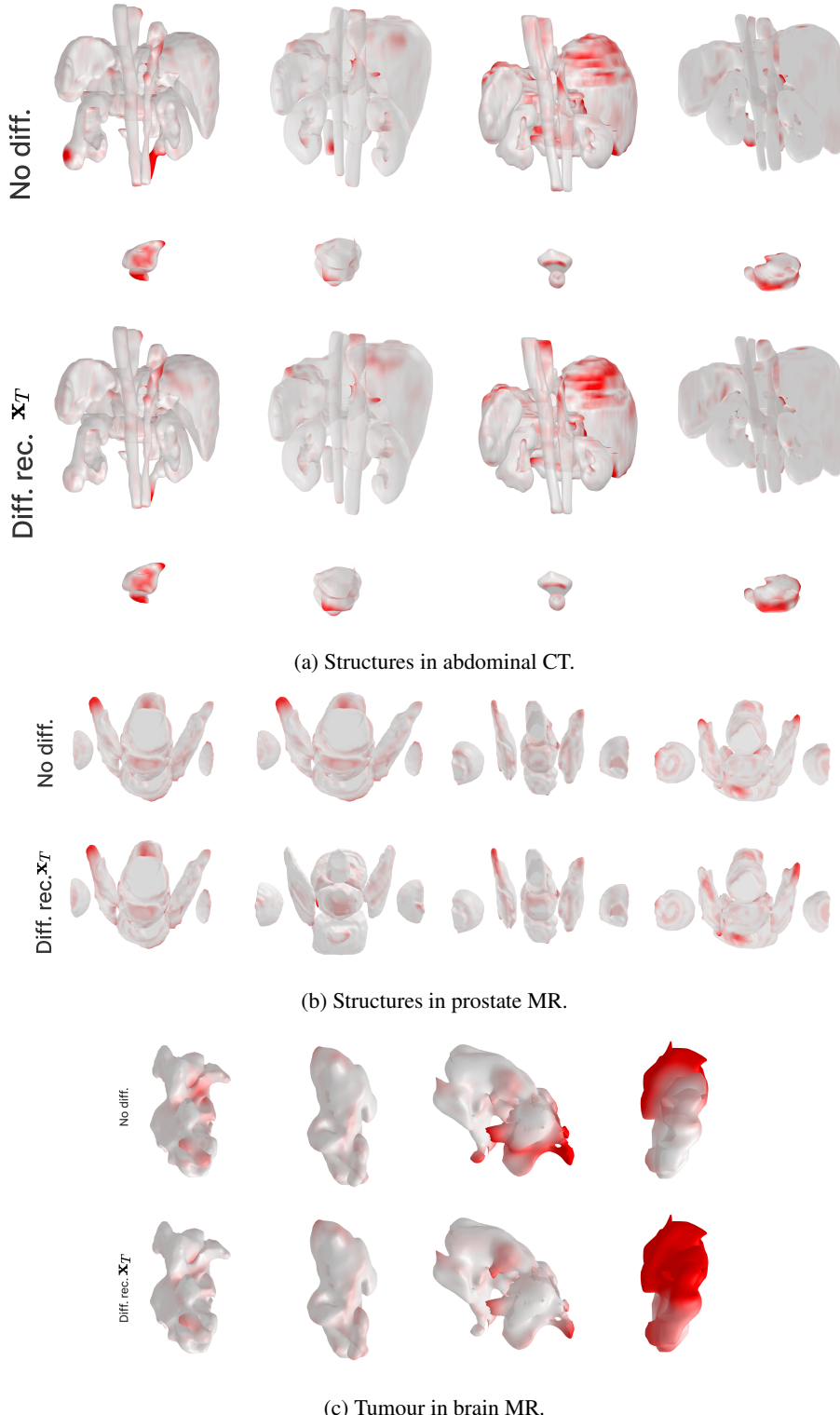


Figure 6: **Segmentation error of non-diffusion-based and diffusion-based models.** “No diff.” represents non-diffusion model. “Diff. rec.  $x_T$ ” represents the diffusion model with proposed recycling. The ground truth segmentation is visualised. For each point on the surface, the distance to the surface of predicted segmentation is calculated and displayed with red color.

Table 5: **Per class segmentation performance comparison for abdominal CT.** “No diff.” represents non-diffusion model. “Diff. rec.  $x_T$ ” represents the diffusion model with proposed recycling. The inference sampler is DDPM. The best results are underlined and a wavy line indicates the difference is significant with  $p\text{-value} < 0.01$ .

Method	Spleen	RT kidney	LT kidney	Gall bladder
Diff. rec. $x_T$	$96.40 \pm 2.42$	<u><math>96.24 \pm 1.90</math></u>	$96.27 \pm 1.53$	$76.68 \pm 29.25$
No diff.	<u><math>96.62 \pm 1.87</math></u>	$95.08 \pm 10.74$	<u><math>96.29 \pm 1.73</math></u>	<u><math>78.83 \pm 27.82</math></u>
Method	Esophagus	Liver	Stomach	Aorta
Diff. rec. $x_T$	<u><math>83.60 \pm 10.32</math></u>	$97.33 \pm 1.13$	$90.77 \pm 14.46$	<u><math>94.66 \pm 4.66</math></u>
No diff.	$83.22 \pm 11.08$	<u><math>97.36 \pm 1.17</math></u>	$90.53 \pm 14.78$	$94.65 \pm 4.22$
Method	Postcava	Pancreas	RT adrenal gland	LT adrenal gland
Diff. rec. $x_T$	<u><math>90.55 \pm 4.19</math></u>	$84.86 \pm 11.15$	$76.63 \pm 12.84$	<u><math>78.01 \pm 11.60</math></u>
No diff.	$90.45 \pm 4.68$	<u><math>84.88 \pm 11.40</math></u>	<u><math>77.80 \pm 9.46</math></u>	<u><math>77.98 \pm 11.95</math></u>
Method	Duodenum	Bladder	Prostate/Uterus	
Diff. rec. $x_T$	<u><math>79.80 \pm 15.14</math></u>	$87.90 \pm 16.65$	$81.90 \pm 18.86$	
No diff.	$79.57 \pm 14.89$	<u><math>88.09 \pm 16.25</math></u>	<u><math>82.35 \pm 18.90</math></u>	

(a) Abdominal CT: Dice score per class. LT and RT stand for left and right, respectively.

Method	Spleen	RT kidney	LT kidney	Gall bladder
Diff. rec. $x_T$	<u><math>2.86 \pm 3.84</math></u>	<u><math>1.93 \pm 0.83</math></u>	$3.13 \pm 8.35$	$12.65 \pm 21.74$
No diff.	$3.22 \pm 4.91$	$1.97 \pm 1.46$	$4.13 \pm 10.83$	<u><math>9.23 \pm 16.71</math></u>
Method	Esophagus	Liver	Stomach	Aorta
Diff. rec. $x_T$	<u><math>5.30 \pm 6.41</math></u>	$3.79 \pm 4.16$	$9.00 \pm 14.03$	<u><math>5.41 \pm 11.20</math></u>
No diff.	$5.50 \pm 6.81$	<u><math>3.50 \pm 2.50</math></u>	<u><math>8.96 \pm 13.99</math></u>	$6.62 \pm 14.52$
Method	Postcava	Pancreas	RT adrenal gland	LT adrenal gland
Diff. rec. $x_T$	<u><math>4.62 \pm 3.09</math></u>	<u><math>7.50 \pm 8.62</math></u>	$4.66 \pm 3.14$	<u><math>4.87 \pm 4.64</math></u>
No diff.	$4.80 \pm 4.55$	$7.57 \pm 8.62$	<u><math>4.39 \pm 2.39</math></u>	$5.15 \pm 5.40$
Method	Duodenum	Bladder	Prostate/uterus	
Diff. rec. $x_T$	<u><math>9.31 \pm 7.13</math></u>	$10.70 \pm 31.83$	$13.35 \pm 32.75$	
No diff.	$10.54 \pm 8.44$	<u><math>9.10 \pm 23.07</math></u>	<u><math>10.97 \pm 19.01</math></u>	

(b) Abdominal CT: Hausdorff distance per class. LT and RT stand for left and right, respectively.

Table 6: **Per class segmentation performance comparison for prostate MR.** “No diff.” represents non-diffusion model. “Diff. rec.  $\mathbf{x}_T$ ” represents the diffusion model with proposed recycling. The inference sampler is DDPM. The best results are underlined and a wavy line indicates the difference is significant with  $p\text{-value} < 0.01$ .

Method	Bladder	Bone	Obturator internus	Transition zone
Diff. rec. $\mathbf{x}_T$	<u><math>93.57 \pm 9.61</math></u>	<u><math>93.84 \pm 5.85</math></u>	<u><math>89.15 \pm 3.62</math></u>	<u><math>79.79 \pm 8.36</math></u>
No diff.	$93.28 \pm 9.90$	$93.12 \pm 5.68$	$88.95 \pm 3.53$	$79.61 \pm 8.37$
Method	Central gland	Rectum	Seminal vesicle	NV bundle
Diff. rec. $\mathbf{x}_T$	<u><math>89.13 \pm 5.78</math></u>	<u><math>93.42 \pm 3.51</math></u>	<u><math>78.39 \pm 9.71</math></u>	<u><math>67.07 \pm 15.50</math></u>
No diff.	$88.75 \pm 5.60$	$93.30 \pm 3.48$	$77.55 \pm 10.99$	$67.17 \pm 14.34$

(a) Prostate MR: Dice score per class. NV stands for neurovascular.

Method	Bladder	Bone	Obturator internus	Transition zone
Diff. rec. $\mathbf{x}_T$	<u><math>3.20 \pm 4.12</math></u>	<u><math>2.21 \pm 1.62</math></u>	<u><math>4.50 \pm 3.46</math></u>	<u><math>6.25 \pm 4.96</math></u>
No diff.	$3.30 \pm 4.54$	$3.18 \pm 9.77$	$4.60 \pm 3.36$	$5.97 \pm 4.97$
Method	Central gland	Rectum	Seminal vesicle	NV bundle
Diff. rec. $\mathbf{x}_T$	<u><math>3.70 \pm 1.93</math></u>	<u><math>4.25 \pm 4.75</math></u>	<u><math>4.57 \pm 2.66</math></u>	<u><math>6.55 \pm 6.28</math></u>
No diff.	$3.94 \pm 2.28$	$4.46 \pm 5.69$	$4.82 \pm 3.85$	$6.68 \pm 6.33$

(b) Prostate MR: Hausdorff distance per class. NV stands for neurovascular.

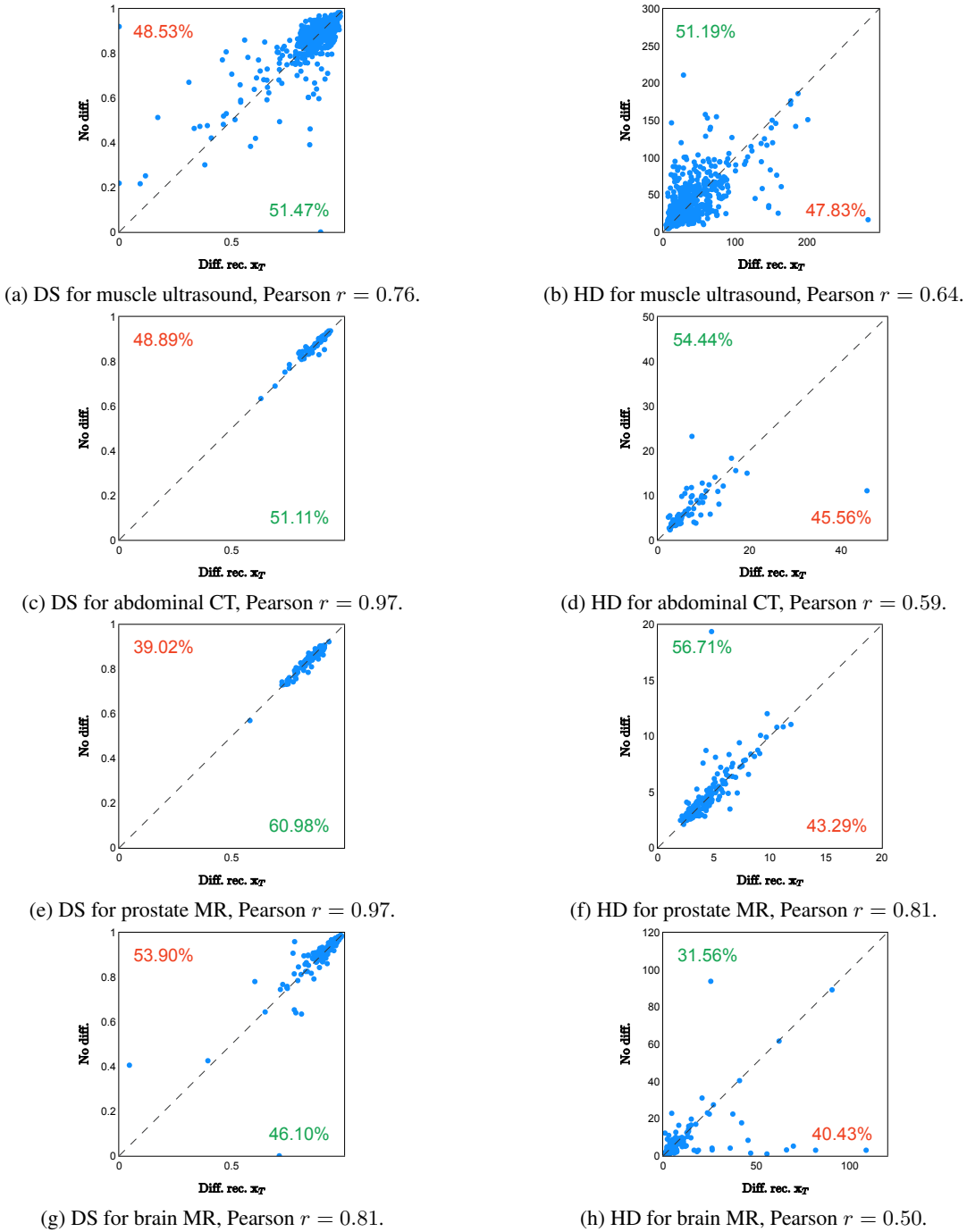


**Figure 7: Per-sample segmentation performance comparison between non-diffusion-based and diffusion-based models.** “No diff.” represents non-diffusion model. “Diff. rec.  $x_T$ ” represents the diffusion model with proposed recycling. The inference sampler is DDPM. DS and HD represents Dice score and Hausdorff distance, respectively. The percentage indicates the number of samples above or below the line  $y = x$ , with green colours indicating diffusion model having better performance. The Pearson correlation between two models has also been computed.

applications. Future research could explore combining or augmenting existing methods with the proposed generative approaches for further performance improvements.

## 6 Conclusion

In this research, we have proposed a novel training strategy for diffusion-based segmentation models. The aim is to remove the dependency on ground truth masks during denoising training. In contrast to the standard diffusion-based segmentation models and those employing self-conditioning or alternative recycling techniques, our approach consistently maintains or enhances segmentation performance throughout progressive inference processes. Through extensive experiments across four medical imaging data sets with different dimensionalities and modalities, we demonstrated statistically significant improvement against all diffusion baseline models for both DDPM and DDIM samplers. Our analysis for the first time identified a common limitation of existing diffusion model training for segmentation tasks. The use of ground truth data for denoising training leads to data leakage. By utilising model’s prediction at the initial step instead, we align the training process with inference procedures, effectively reducing over-fitting and promoting better generalization. While existing diffusion models underperformed non-diffusion-based segmentation model baselines, our innovative recycling training strategies effectively bridged the performance gap. This enhancement allowed diffusion models to attain comparable performance levels. To the best of our knowledge, this is the first time diffusion models achieve such parity in performance while maintaining identical architecture and compute budget. Nevertheless, challenges remain on the road to advancing diffusion-based segmentation models further. Future work could explore discrete diffusion models which are tailored for categorical data or implement diffusion in latent space to further reduce compute costs. Although the presented experimental results primarily demonstrated methodological development, the fact that these were obtained on four large clinical data sets represents a promising step towards real-world applications. We would like to argue the potential importance in the reported development, which may lead to better clinical outcome and improved patient care in respective applications. For example, avoiding surrounding healthy structures may be sensitive to their localisation in planning imaging, in both the abdominal CT and prostate MR tasks. This sensitivity can be high and nonlinear therefore arguably a perceived marginal improvement might benefit those with smaller targets, such as those in liver resection and focal therapy of prostate cancer, or highly variable ultrasound imaging guidance.

## 7 Acknowledgement

This work was supported by the EPSRC grant (EP/T029404/1), the Wellcome/EPSRC Centre for Interventional and Surgical Sciences (203145Z/16/Z), the International Alliance for Cancer Early Detection, an alliance between Cancer Research UK (C28070/A30912, C73666/A31378), Canary Center at Stanford University, the University of Cambridge, OHSU Knight Cancer Institute, University College London and the University of Manchester, and Cloud TPUs from Google’s TPU Research Cloud (TRC).

## 8 Ethics

The work follows appropriate ethical standards in conducting research and writing the manuscript, following all applicable laws and regulations regarding treatment of animals or human subjects.

## 9 Conflict of Interest

We declare we do not have conflicts of interest.

## References

- Jascha Sohl-Dickstein, Eric Weiss, Niru Maheswaranathan, and Surya Ganguli. Deep unsupervised learning using nonequilibrium thermodynamics. In *International Conference on Machine Learning*, pages 2256–2265. PMLR, 2015.
- Jonathan Ho, Ajay Jain, and Pieter Abbeel. Denoising diffusion probabilistic models. *Advances in Neural Information Processing Systems*, 33:6840–6851, 2020.
- Jonathan Ho and Tim Salimans. Classifier-free diffusion guidance. *arXiv preprint arXiv:2207.12598*, 2022.
- Ian Goodfellow, Jean Pouget-Abadie, Mehdi Mirza, Bing Xu, David Warde-Farley, Sherjil Ozair, Aaron Courville, and Yoshua Bengio. Generative adversarial networks. *Communications of the ACM*, 63(11):139–144, 2020.

- Aditya Ramesh, Prafulla Dhariwal, Alex Nichol, Casey Chu, and Mark Chen. Hierarchical text-conditional image generation with clip latents. [arXiv preprint arXiv:2204.06125](#), 2022.
- Robin Rombach, Andreas Blattmann, Dominik Lorenz, Patrick Esser, and Björn Ommer. High-resolution image synthesis with latent diffusion models. In [Proceedings of the IEEE/CVF Conference on Computer Vision and Pattern Recognition](#), pages 10684–10695, 2022.
- Zolnamar Dorjsembe, Sodtavilan Odonchimed, and Furen Xiao. Three-dimensional medical image synthesis with denoising diffusion probabilistic models. In [Medical Imaging with Deep Learning](#), 2022.
- Firas Khader, Gustav Mueller-Franzes, Soroosh Tayebi Arasteh, Tianyu Han, Christoph Haarburger, Maximilian Schulze-Hagen, Philipp Schad, Sandy Engelhardt, Bettina Baessler, Sebastian Foersch, et al. Medical diffusion-denoising diffusion probabilistic models for 3d medical image generation. [arXiv preprint arXiv:2211.03364](#), 2022.
- Dewei Hu, Yuankai K Tao, and Ipek Oguz. Unsupervised denoising of retinal oct with diffusion probabilistic model. In [Medical Imaging 2022: Image Processing](#), volume 12032, pages 25–34. SPIE, 2022.
- Julia Wolleb, Florentin Bieder, Robin Sandkühler, and Philippe C Cattin. Diffusion models for medical anomaly detection. In [International Conference on Medical image computing and computer-assisted intervention](#), pages 35–45. Springer, 2022a.
- Yijun Yang, Huazhu Fu, Angelica Aviles-Rivero, Carola-Bibiane Schönlieb, and Lei Zhu. Diffmic: Dual-guidance diffusion network for medical image classification. [arXiv preprint arXiv:2303.10610](#), 2023.
- Junde Wu, Huihui Fang, Yu Zhang, Yehui Yang, and Yanwu Xu. Medsegdiff: Medical image segmentation with diffusion probabilistic model. [arXiv preprint arXiv:2211.00611](#), 2022.
- Aimon Rahman, Jeya Maria Jose Valanarasu, Ilker Hacihaliloglu, and Vishal M Patel. Ambiguous medical image segmentation using diffusion models. In [Proceedings of the IEEE/CVF Conference on Computer Vision and Pattern Recognition](#), pages 11536–11546, 2023.
- Boah Kim, Inhwa Han, and Jong Chul Ye. Diffusemorph: unsupervised deformable image registration using diffusion model. In [European Conference on Computer Vision](#), pages 347–364. Springer, 2022.
- Zhaohu Xing, Liang Wan, Huazhu Fu, Guang Yang, and Lei Zhu. Diff-unet: A diffusion embedded network for volumetric segmentation. [arXiv preprint arXiv:2303.10326](#), 2023.
- Lukas Zbinden, Lars Doorenbos, Theodoros Pissas, Raphael Sznitman, and Pablo Márquez-Neila. Stochastic segmentation with conditional categorical diffusion models. [arXiv preprint arXiv:2303.08888](#), 2023.
- Junde Wu, Rao Fu, Huihui Fang, Yu Zhang, and Yanwu Xu. Medsegdiff-v2: Diffusion based medical image segmentation with transformer. [arXiv preprint arXiv:2301.11798](#), 2023.
- Yunguan Fu, Yiwen Li, Shaheer U Saeed, Matthew J Clarkson, and Yipeng Hu. Importance of aligning training strategy with evaluation for diffusion models in 3d multiclass segmentation. [arXiv preprint arXiv:2303.06040](#), 2023.
- Walter HL Pinaya, Mark S Graham, Robert Gray, Pedro F Da Costa, Petru-Daniel Tudosi, Paul Wright, Yee H Mah, Andrew D MacKinnon, James T Teo, Rolf Jager, et al. Fast unsupervised brain anomaly detection and segmentation with diffusion models. In [International Conference on Medical Image Computing and Computer-Assisted Intervention](#), pages 705–714. Springer, 2022a.
- Julia Wolleb, Robin Sandkühler, Florentin Bieder, Philippe Valmaggia, and Philippe C Cattin. Diffusion models for implicit image segmentation ensembles. In [International Conference on Medical Imaging with Deep Learning](#), pages 1336–1348. PMLR, 2022b.
- Florentin Bieder, Julia Wolleb, Alicia Durrer, Robin Sandkühler, and Philippe C Cattin. Diffusion models for memory-efficient processing of 3d medical images. [arXiv preprint arXiv:2303.15288](#), 2023.
- Risheng Wang, Tao Lei, Ruixia Cui, Bingtao Zhang, Hongying Meng, and Asoke K Nandi. Medical image segmentation using deep learning: A survey. [IET Image Processing](#), 16(5):1243–1267, 2022.
- Tomer Amit, Eliya Nachmani, Tal Shaharbany, and Lior Wolf. Segdiff: Image segmentation with diffusion probabilistic models. [arXiv preprint arXiv:2112.00390](#), 2021.
- Benedikt Kolbeinsson and Krystian Mikolajczyk. Multi-class segmentation from aerial views using recursive noise diffusion. [arXiv preprint arXiv:2212.00787](#), 2022.
- Diederik Kingma, Tim Salimans, Ben Poole, and Jonathan Ho. Variational diffusion models. [Advances in neural information processing systems](#), 34:21696–21707, 2021.
- Ting Chen, Lala Li, Saurabh Saxena, Geoffrey Hinton, and David J Fleet. A generalist framework for panoptic segmentation of images and videos. [arXiv preprint arXiv:2210.06366](#), 2022a.

- Ting Chen, Ruixiang Zhang, and Geoffrey Hinton. Analog bits: Generating discrete data using diffusion models with self-conditioning. [arXiv preprint arXiv:2208.04202](#), 2022b.
- Joseph L Watson, David Juergens, Nathaniel R Bennett, Brian L Trippe, Jason Yim, Helen E Eisenach, Woody Ahern, Andrew J Borst, Robert J Ragotte, Lukas F Milles, et al. De novo design of protein structure and function with rfdiffusion. [Nature](#), pages 1–3, 2023.
- Jiaming Song, Chenlin Meng, and Stefano Ermon. Denoising diffusion implicit models. [arXiv preprint arXiv:2010.02502](#), 2020a.
- Aapo Hyvärinen and Peter Dayan. Estimation of non-normalized statistical models by score matching. [Journal of Machine Learning Research](#), 6(4), 2005.
- Pascal Vincent. A connection between score matching and denoising autoencoders. [Neural computation](#), 23(7): 1661–1674, 2011.
- Yang Song and Stefano Ermon. Generative modeling by estimating gradients of the data distribution. [Advances in neural information processing systems](#), 32, 2019.
- Yang Song and Stefano Ermon. Improved techniques for training score-based generative models. [Advances in neural information processing systems](#), 33:12438–12448, 2020.
- Alexander Quinn Nichol and Prafulla Dhariwal. Improved denoising diffusion probabilistic models. In [International Conference on Machine Learning](#), pages 8162–8171. PMLR, 2021.
- Luping Liu, Yi Ren, Zhijie Lin, and Zhou Zhao. Pseudo numerical methods for diffusion models on manifolds. [arXiv preprint arXiv:2202.09778](#), 2022.
- Huangjie Zheng, Pengcheng He, Weizhu Chen, and Mingyuan Zhou. Truncated diffusion probabilistic models. [stat](#), 1050:7, 2022.
- Zhaoyang Lyu, Xudong Xu, Ceyuan Yang, Dahua Lin, and Bo Dai. Accelerating diffusion models via early stop of the diffusion process. [arXiv preprint arXiv:2205.12524](#), 2022.
- Xutao Guo, Yanwu Yang, Chenfei Ye, Shang Lu, Yang Xiang, and Ting Ma. Accelerating diffusion models via pre-segmentation diffusion sampling for medical image segmentation. [arXiv preprint arXiv:2210.17408](#), 2022.
- Amirhossein Kazerouni, Ehsan Khodapanah Aghdam, Moein Heidari, Reza Azad, Mohsen Fayyaz, Ilker Hacihaliloglu, and Dorit Merhof. Diffusion models in medical imaging: A comprehensive survey. [Medical Image Analysis](#), page 102846, 2023.
- Yang Song, Jascha Sohl-Dickstein, Diederik P Kingma, Abhishek Kumar, Stefano Ermon, and Ben Poole. Score-based generative modeling through stochastic differential equations. [arXiv preprint arXiv:2011.13456](#), 2020b.
- Prafulla Dhariwal and Alexander Nichol. Diffusion models beat gans on image synthesis. [Advances in Neural Information Processing Systems](#), 34:8780–8794, 2021.
- Walter HL Pinaya, Petru-Daniel Tudosi, Jessica Dafflon, Pedro F da Costa, Virginia Fernandez, Parashkev Nachev, Sébastien Ourselin, and M Jorge Cardoso. Brain imaging generation with latent diffusion models. [arXiv preprint arXiv:2209.07162](#), 2022b.
- Puria Azadi Moghadam, Sanne Van Dalen, Karina C Martin, Jochen Lennerz, Stephen Yip, Hossein Farahani, and Ali Bashashati. A morphology focused diffusion probabilistic model for synthesis of histopathology images. In [Proceedings of the IEEE/CVF Winter Conference on Applications of Computer Vision](#), pages 2000–2009, 2023.
- Shaheer U. Saeed, Tom Syer, Wen Yan, Qianye Yang, Mark Emberton, Shonit Punwani, Matthew J. Clarkson, Dean C. Barratt, and Yipeng Hu. Bi-parametric prostate mr image synthesis using pathology and sequence-conditioned stable diffusion. [arXiv preprint arXiv:2303.02094](#), 2023.
- Xiaochuang Han, Sachin Kumar, and Yulia Tsvetkov. Ssd-lm: Semi-autoregressive simplex-based diffusion language model for text generation and modular control. [arXiv preprint arXiv:2210.17432](#), 2022.
- Xiang Li, John Thickstun, Ishaan Gulrajani, Percy S Liang, and Tatsunori B Hashimoto. Diffusion-lm improves controllable text generation. [Advances in Neural Information Processing Systems](#), 35:4328–4343, 2022a.
- Robin Strudel, Corentin Tallec, Florent Altché, Yilun Du, Yaroslav Ganin, Arthur Mensch, Will Grathwohl, Nikolay Savinov, Sander Dieleman, Laurent Sifre, et al. Self-conditioned embedding diffusion for text generation. [arXiv preprint arXiv:2211.04236](#), 2022.
- Emiel Hoogeboom, Didrik Nielsen, Priyank Jaini, Patrick Forré, and Max Welling. Argmax flows and multinomial diffusion: Learning categorical distributions. [Advances in Neural Information Processing Systems](#), 34:12454–12465, 2021.

- Jacob Austin, Daniel D Johnson, Jonathan Ho, Daniel Tarlow, and Rianne Van Den Berg. Structured denoising diffusion models in discrete state-spaces. *Advances in Neural Information Processing Systems*, 34:17981–17993, 2021.
- Shuyang Gu, Dong Chen, Jianmin Bao, Fang Wen, Bo Zhang, Dongdong Chen, Lu Yuan, and Baining Guo. Vector quantized diffusion model for text-to-image synthesis. In *Proceedings of the IEEE/CVF Conference on Computer Vision and Pattern Recognition*, pages 10696–10706, 2022.
- Tao Chen, Chenhui Wang, and Hongming Shan. Berdiff: Conditional bernoulli diffusion model for medical image segmentation. [arXiv preprint arXiv:2304.04429](#), 2023.
- Hefeng Wang, Jiale Cao, Rao Muhammad Anwer, Jin Xie, Fahad Shahbaz Khan, and Yanwei Pang. Dformer: Diffusion-guided transformer for universal image segmentation. [arXiv preprint arXiv:2306.03437](#), 2023.
- Zeqiang Lai, Yuchen Duan, Jifeng Dai, Ziheng Li, Ying Fu, Hongsheng Li, Yu Qiao, and Wenhui Wang. Denoising diffusion semantic segmentation with mask prior modeling. [arXiv preprint arXiv:2306.01721](#), 2023.
- Sean I Young, Adrian V Dalca, Enzo Ferrante, Polina Golland, Bruce Fischl, and Juan Eugenio Iglesias. Sud: Supervision by denoising for medical image segmentation. [arXiv preprint arXiv:2202.02952](#), 2022.
- Francesco Marzola, Nens van Alfen, Jonne Doorduin, and Kristen M Meiburger. Deep learning segmentation of transverse musculoskeletal ultrasound images for neuromuscular disease assessment. *Computers in Biology and Medicine*, 135:104623, 2021.
- Ujjwal Baid, Satyam Ghodasara, Suyash Mohan, Michel Bilello, Evan Calabrese, Errol Colak, Keyvan Farahani, Jayashree Kalpathy-Cramer, Felipe C Kitamura, Sarthak Pati, et al. The rsna-asnr-miccai brats 2021 benchmark on brain tumor segmentation and radiogenomic classification. [arXiv preprint arXiv:2107.02314](#), 2021.
- Yuanfeng Ji, Haotian Bai, Jie Yang, Chongjian Ge, Ye Zhu, Ruimao Zhang, Zhen Li, Lingyan Zhang, Wanling Ma, Xiang Wan, et al. Amos: A large-scale abdominal multi-organ benchmark for versatile medical image segmentation. [arXiv preprint arXiv:2206.08023](#), 2022.
- Yiwen Li, Yunguan Fu, Iani Gayo, Qianye Yang, Zhe Min, Shaheer Saeed, Wen Yan, Yipei Wang, J Alison Noble, Mark Emberton, et al. Prototypical few-shot segmentation for cross-institution male pelvic structures with spatial registration. [arXiv preprint arXiv:2209.05160](#), 2022b.
- Alexander Kirillov, Eric Mintun, Nikhila Ravi, Hanzi Mao, Chloe Rolland, Laura Gustafson, Tete Xiao, Spencer Whitehead, Alexander C Berg, Wan-Yen Lo, et al. Segment anything. [arXiv preprint arXiv:2304.02643](#), 2023.

## A Tables

Table 7: Training Hyper-parameters.

Parameter	Value
Optimiser	AdamW (b1=0.9, b2=0.999, weight_decay=1E-8)
Learning Rate Warmup	100 steps
Learning Rate Decay	10,000 steps
Learning Rate Values	Initial = 1E-5, Peak = 8E-4, End = 5E-5
Batch size	256 for Muscle Ultrasound and 8 for other data sets
Number of samples	320K for Muscle Ultrasound and 100K for other data sets

Table 8: **Diffusion with different training variance schedule.** “Diff.” represents standard diffusion. “sc.  $\mathbf{x}_t$ ” and “sc.  $\mathbf{x}_{t+1}$ ” represents self-conditioning from Chen et al. [2022b] and Watson et al. [2023], respectively. “rec.  $\mathbf{x}_{t+1}$ ” and “rec.  $\mathbf{x}_T$ ” represents recycling from Fu et al. [2023] and the proposed recycling in this work, respectively. “T” represents the length of variance schedule during training. The best results are underlined and a wavy line indicates the difference to the second best is significant with p-value  $< 0.01$ .

T	Method	DDPM		DDIM	
		DS $\uparrow$	HD $\downarrow$	DS $\uparrow$	HD $\downarrow$
1001	Diff.	$86.60 \pm 12.38$	$41.11 \pm 35.48$	$86.18 \pm 12.41$	$42.31 \pm 35.82$
	Diff. sc. $\mathbf{x}_t$	$86.35 \pm 14.14$	$40.42 \pm 37.53$	$85.96 \pm 13.78$	$42.00 \pm 36.76$
	Diff. sc. $\mathbf{x}_{t+1}$	$87.14 \pm 11.48$	$39.24 \pm 32.83$	$86.30 \pm 11.49$	$41.89 \pm 32.72$
	Diff. rec. $\mathbf{x}_{t+1}$	$87.44 \pm 12.39$	$39.68 \pm 36.21$	$87.43 \pm 12.25$	$39.82 \pm 35.39$
	Diff. rec. $\mathbf{x}_T$	$88.23 \pm 11.69$	$35.37 \pm 31.79$	$88.21 \pm 11.70$	$35.52 \pm 31.91$
5	Diff.	$87.81 \pm 10.98$	$37.39 \pm 31.17$	$87.76 \pm 11.00$	$37.56 \pm 31.34$
	Diff. sc. $\mathbf{x}_t$	$88.11 \pm 11.06$	$35.94 \pm 30.13$	$88.20 \pm 10.73$	$35.57 \pm 29.68$
	Diff. sc. $\mathbf{x}_{t+1}$	$87.61 \pm 10.88$	$37.76 \pm 29.91$	$88.09 \pm 10.66$	$35.73 \pm 29.26$
	Diff. rec. $\mathbf{x}_{t+1}$	$88.19 \pm 10.60$	$36.10 \pm 30.38$	$87.83 \pm 11.01$	$37.22 \pm 30.55$
	Diff. rec. $\mathbf{x}_T$	$89.01 \pm 10.79$	$33.70 \pm 30.29$	$88.80 \pm 11.54$	$34.26 \pm 31.88$

(a) Muscle Ultrasound

T	Method	DDPM		DDIM	
		DS $\uparrow$	HD $\downarrow$	DS $\uparrow$	HD $\downarrow$
1001	Diff.	$85.25 \pm 5.36$	$7.12 \pm 3.83$	$85.59 \pm 5.24$	$7.13 \pm 3.98$
	Diff. sc. $\mathbf{x}_t$	$86.04 \pm 5.12$	$7.06 \pm 4.20$	$85.50 \pm 5.14$	$7.21 \pm 4.16$
	Diff. sc. $\mathbf{x}_{t+1}$	$85.86 \pm 5.27$	$6.98 \pm 3.54$	$85.25 \pm 5.42$	$7.28 \pm 3.72$
	Diff. rec. $\mathbf{x}_{t+1}$	$86.48 \pm 5.24$	$6.69 \pm 4.59$	$86.35 \pm 5.31$	$6.75 \pm 4.55$
	Diff. rec. $\mathbf{x}_T$	$87.45 \pm 5.43$	$6.56 \pm 5.44$	$87.45 \pm 5.43$	$6.55 \pm 5.43$
5	Diff.	$86.42 \pm 5.00$	$7.09 \pm 4.40$	$86.52 \pm 5.18$	$6.65 \pm 3.88$
	Diff. sc. $\mathbf{x}_t$	$86.68 \pm 4.96$	$7.06 \pm 6.98$	$86.39 \pm 4.87$	$7.12 \pm 6.95$
	Diff. sc. $\mathbf{x}_{t+1}$	$86.34 \pm 5.33$	$6.69 \pm 3.46$	$86.13 \pm 5.27$	$6.74 \pm 3.55$
	Diff. rec. $\mathbf{x}_{t+1}$	$87.27 \pm 5.20$	$6.64 \pm 4.69$	$87.27 \pm 5.20$	$6.63 \pm 4.69$
	Diff. rec. $\mathbf{x}_T$	$87.38 \pm 5.46$	$6.71 \pm 4.46$	$87.37 \pm 5.45$	$6.74 \pm 4.49$

(b) Abdominal CT

## B Figures

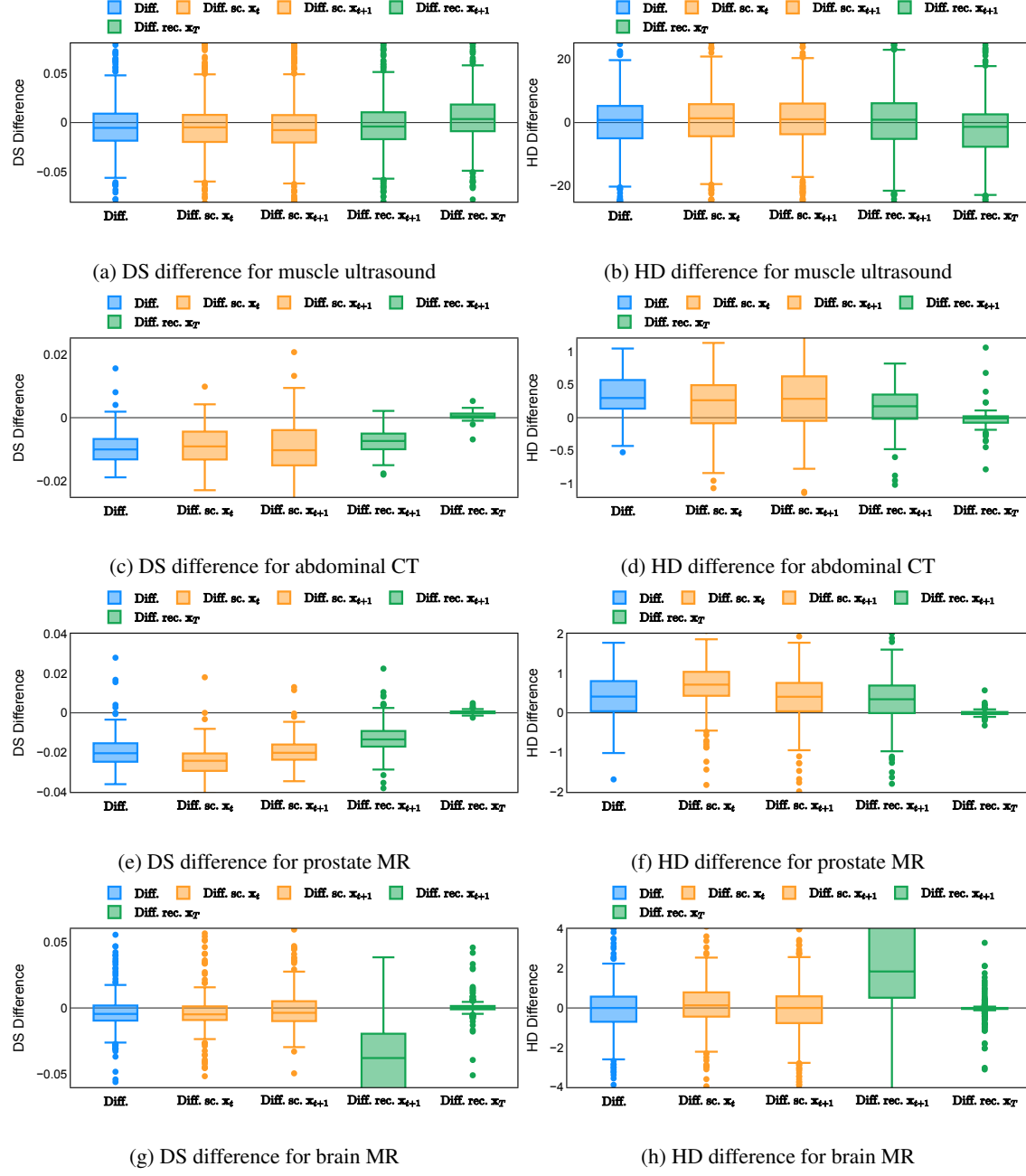


Figure 8: **Segmentation performance per step.** “Diff.” represents standard diffusion. “sc.  $x_t$ ” and “sc.  $x_{t+1}$ ” represents self-conditioning from Chen et al. [2022b] and Watson et al. [2023], respectively. “rec.  $x_{t+1}$ ” and “rec.  $x_T$ ” represents recycling from Fu et al. [2023] and the proposed recycling in this work, respectively. The sampler is DDIM. DS and HD represents Dice score and Hausdorff distance, respectively. The difference is the value at the last step subtracted by the one at the first step. A positive value for Dice score difference or a negative value for Hausdorff distance means improvement.

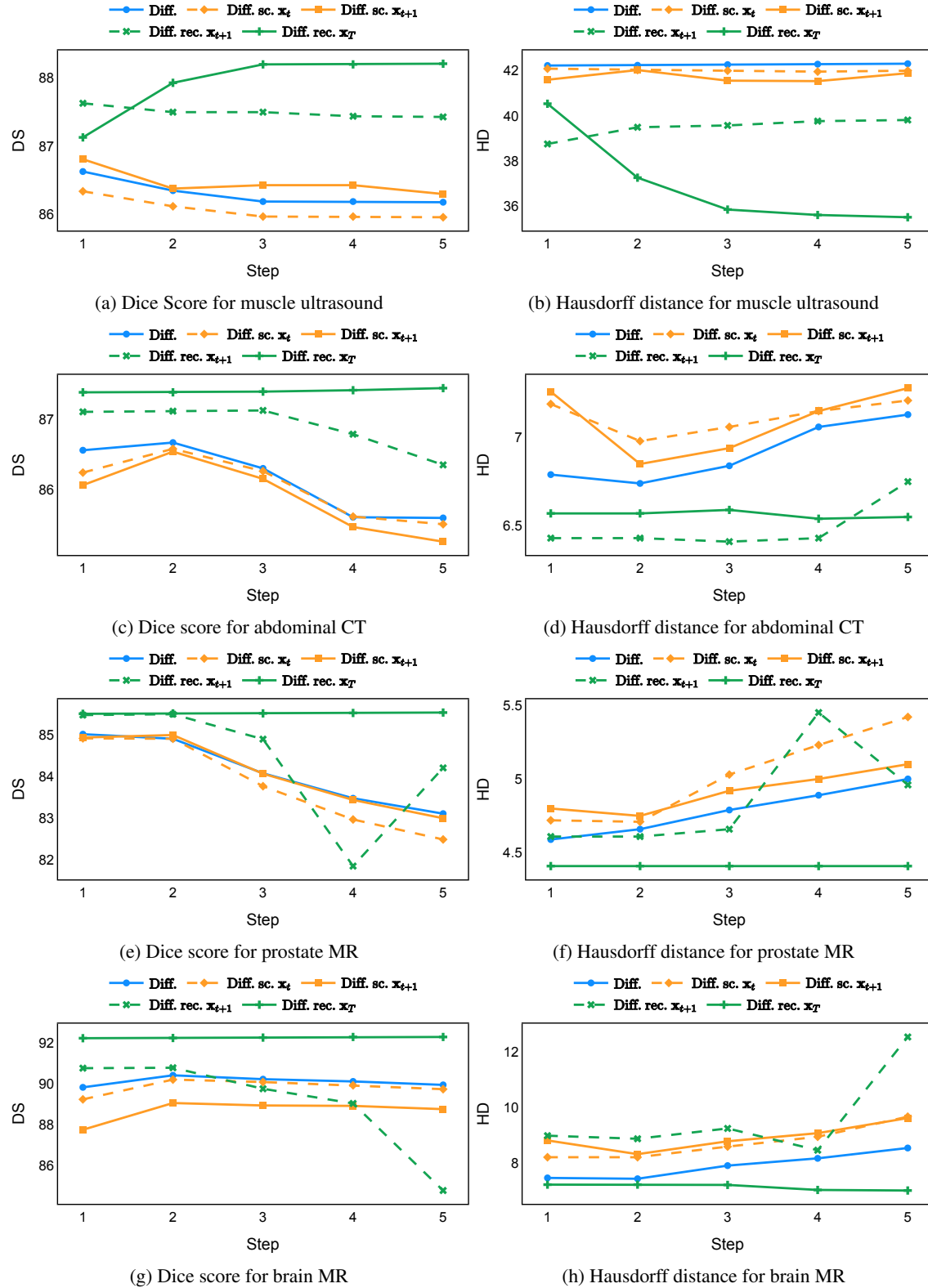


Figure 9: **Segmentation performance per step.** “Diff.” represents standard diffusion. “sc.  $x_t$ ” and “sc.  $x_{t+1}$ ” represents self-conditioning from Chen et al. [2022b] and Watson et al. [2023], respectively. “rec.  $x_{t+1}$ ” and “rec.  $x_T$ ” represents recycling from Fu et al. [2023] and the proposed recycling in this work, respectively. The sampler is DDIM.